Cronfa - Swansea University Open Access Repository

_____

This is an author produced version of a paper published in :
Materials Science and Engineering: A

_____

Cronfa URL for this paper:

http://cronfa.swan.ac.uk/Record/cronfa30238

_____

Paper:

_____

Author's Accepted Manuscript

Effects of hot isostatic pressing on the elastic modulus and tensile properties of 316L parts made by powder bed laser fusion

N.P. Lavery, J. Cherry, S. Mehmood, H. Davies, B. Girling, E. Sacket, S.G.R. Brown, J. Sienz

MATERIALS SCIENCE & ENGINEERING

A

Structural Materials: Properties, Microstructure and Processing

Editor in Chief:
E.J. Lavernia

Editors:
E. Werner
M. Starink
J.D. Whittenberger
J.K. Shang

Available online at sciencedirect.com
SciVerse ScienceDirect

www.elsevier.com/locate/msea

Cite this article as: N.P. Lavery, J. Cherry, S. Mehmood, H. Davies, B. Girling, E. Sacket, S.G.R. Brown and J. Sienz, Effects of hot isostatic pressing on the elastic modulus and tensile properties of 316L parts made by powder bed laser fusion, *Materials Science & Engineering A*, http://dx.doi.org/10.1016/j.msea.2017.03.100
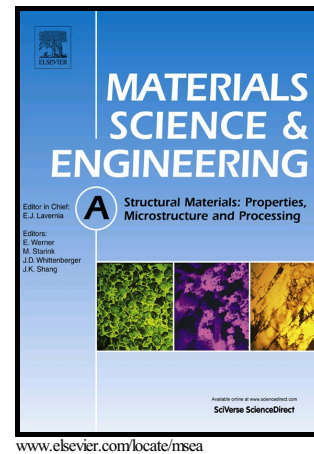
This is a PDF file of an unedited manuscript that has been accepted for publication. As a service to our customers we are providing this early version of the manuscript. The manuscript will undergo copyediting, typesetting, and review of the resulting galley proof before it is published in its final citable form. Please note that during the production process errors may be discovered which could affect the content, and all legal disclaimers that apply to the journal pertain.

Effects of hot isostatic pressing on the elastic modulus and tensile properties of 316L parts made by powder bed laser fusion

N. P. Lavery[A*], J. Cherry, S. Mehmood, H. Davies [A], B. Girling, E. Sacket, S.G.R. Brown [A], J. Sienz [B]

[A] *Materials Research Centre, College of Engineering, Swansea University Bay Campus, Fabian Way, Swansea SA1 8EP, United Kingdom*
[B] *Zienkiewicz Centre for Computational Engineering, College of Engineering, Swansea University Bay Campus, Fabian Way, Swansea SA1 8EP, United Kingdom*

[*]Corresponding author, Tel: +44(0)1792 606873. N.P.Lavery@swansea.ac.uk

Abstract

The microstructure and mechanical properties of 316L steel have been examined for parts built by a powder bed laser fusion process, which uses a laser to melt and build parts additively on a layer by layer basis.

Relative density and porosity determined using various experimental techniques were correlated against laser energy density. Based on porosity sizes, morphology and distributions, the porosity was seen to transition between an irregular, highly directional porosity at the low laser energy density and a smaller, more rounded and randomly distributed porosity at higher laser energy density, thought to be caused by keyhole melting. In both cases, the porosity was reduced by hot isostatic pressing (HIP).

High throughput ultrasound based measurements were used to calculate elasticity properties and show that the lower porosities from builds with higher energy densities have higher elasticity moduli in accordance with empirical relationships, and hot isostatic pressing improves the elasticity properties to levels associated with wrought/rolled 316L. However, even with hot isostatic pressing the best properties were obtained from samples with the lowest porosity in the as-built condition.

A finite element stress analysis based on the porosity microstructures was undertaken, to understand the effect of pore size distributions and morphology on the Young's modulus. Over 1-5% porosity range angular porosity was found to reduce the Young's modulus by 5% more than rounded porosity. Experimentally measured Young's moduli for samples treated by HIP were closer to the rounded trends than the as-built samples, which were closer to angular trends.

Tensile tests on specimens produced at optimised machine parameters displayed a high degree of anisotropy in the build direction and test variability for as-built parts, especially between vertical and horizontal build directions. The as-built properties were generally found to have a higher yield stress, but lower upper tensile strength and elongation than published data for wrought/hot-rolled plate 316L. The hot isostatically pressed parts showed a homogenisation of the properties across build directions and properties much more akin to those of wrought/hot-rolled 316L, with an increase in elongation and upper tensile strength, and a reduction in yield over the as-built samples.

Keywords: Powder Bed Laser Fusion, 316L steel, Porosity, Hot Isostatic Pressing, Tensile, Ultrasound Measurements of Elasticity, Finite Element Analysis

1 Introduction

Additive Layer Manufacturing (ALM) based on the melting of pre-alloyed metal powders is a processing route which is rapidly evolving from rapid prototyping with the capability of producing functional net-shape parts with the strength characteristics of wrought parts [1]. It is ideally suited to low-volume production, and can be cost-competitive or cheaper than CNC machining or processes where the capital outlay for items such as dies are high [2]. However, as with all powder-based processes, such as sintering [3], net-shape hot isostatic pressing [4], and powder compaction [5], as well as other net-shape manufacturing methods such as casting [6], there is an inherent porosity associated with the process.

The literature is rich in studies reporting on specific combinations of alloys, ALM techniques and applications. Titanium alloys, such as Ti-6Al-4V are being examined for use as critical aerospace and biomedical applications such as orthopaedic devices, and dental implants, and are understandably receiving a large proportion of the effort.

Typically the material/process development cycle will start by studying the links between porosity and tensile strength, as exemplified for powder bed fusion processes, of which selective laser melting (SLM) generally referrers to processes specifically using optical based lasers, [7], wire-feed processes [8] and electron beam processes, [1], [9]–[11]. Common conclusions from this type of work are that anisotropic mechanical properties occur to a varying degree, and that there are also various levels of porosity which have a detrimental effect on ductility, accompanied by high levels of hardness and yield strength.

The effects on mechanical properties of surface finishing, heat treatments and hot isostatic pressing are then examined, and for Ti-6Al-4V this is done for powder bed [7], [12] and for electron beam [11]. Due to the relatively rough surfaces of additive processes, surface finishing such as polishing or machining can improve mechanical properties, particularly fatigue strength [4], [11], [13].

For Ti-6Al-4V, heat treatments such as aging and annealing for stress reduction are found to have relatively small effects on mechanical properties, slightly increasing ductility and reducing anisotropy, with some reduction in the yield strength. Generally, more aggressive heat treatments and hot isostatic pressing give a larger reduction in sometimes both yield and upper tensile strength, and are accompanied by an increase in ductility and a reduction in build direction anisotropy, often associated with the adequate closure of small porosity in the case of hot isostatic pressing. This is also the case for nickel alloys such as Inconel 718 [14], [15], although in the case of this alloy the ductility can be reduced with heat treatment as a consequence of an acicular δ-phase migrating to grain boundaries. Nickel alloys have also been subject to studies with intended applications in aerospace, concentrating on the microstructural characterisation and effects on mechanical strength of parts build by the powder bed fusion process with Inconel 718, [16] and Nimonic 273, [17], both examining the post-modification by heat treatment of the as-built part.

Heat treatments have significantly more effect on commonly used aluminium alloys such as AlSi10 [18]–[22] and AlSi12 [23], often intended for automotive and electronic applications, and much of the current focus of powder bed based ALM research using aluminium has been on the Al-Si casting alloys, such as AlSi10, [19], which although possibly easier to process than high strength aerospace Al-alloy grades due to narrower freezing ranges, still pose significant challenges when compared to

steels and other higher melting point alloys. High strength aluminium alloys (5XXX and 7XXX-series) are also being considered [24] for aerospace applications for powder bed ALM, and modified compositions such as with higher scandium content,[25] are showing acceptable porosity and promising strength and ductility characteristics. Porosity fractions of aluminium alloys can be reduced to less than 0.5%, certainly comparable to casting routes with fewer inclusions and defects, however, pore sizes tend to be larger than with other ALM alloys, with overall static strength tests showing higher tensile and fatigue strength than cast materials, [22].

Fatigue strength requires longer term tests, which tend to come later in the material/process development cycle, and fatigue studies have been reported for Ti-6Al-4V in [20], [26], [27], steels [13], [28] and aluminium alloys [20], [22]. Generally the findings are that while heat treatments and hot isostatic pressing can improve fatigue strength, that mostly these still be below 60-75% of an equivalent wrought, annealed material.

Although much work has already been done on duplex steels such as 304 and 316L on a variety of powder bed systems, [29], [20], [30]–[38], the published data covers a wide range of preparation routes, machine settings and laser powers, different mechanical testing methodologies and various post-process heat treatments. Unlike higher strength H13 and maraging steels such as 18Ni-300, [39] which are used in injection moulding tools and dies, and aeroengine applications, the lower strength 316L is widely used but does not have any one single critical application possibly explaining the wide range of research interests. However, this poses a difficulty in setting a baseline for the required tensile properties of 316L, as demonstrated by the limited validation in the publications comparing ALM with other processes such as hot rolling, wrought or casting.

As pointed out in [20], the proliferation and progress of additive processes means that the mechanical characterisation even for standard alloys struggles to keep pace with the machine developments. This is very evident in the case of 316L steel where even recent publications are reporting tensile properties for samples built with the previous generation of powder bed systems, with low laser powers (85-200W) and line speeds (down to 200 mm/s), and wider ranges of porosity (1-3%). Laser powers of 500W and line speeds of 2-3000 mm/s are the norm in the current generation of machines, resulting in lower levels of porosity (0.1-0.5%) expected across all alloys.

The work reported herein aims to add to the body of knowledge on 316L with an in-depth characterisation of the material for a 200W laser machine, at line speeds in the 600-1000 mm/s range. The claim to be in-depth is based on a thorough description of the measurement methodologies (density, porosity and tensile properties), for both as-built and hot isostatically pressed samples, to be a baseline for future researchers. It also introduces the use of ultrasound testing which has seen a limited amount of use in ALM materials characterisation even though it is a more rapid method of getting elasticity properties than through tensile testing. It is thought that ultrasound techniques can contribute to process improvement, such as by reducing directional variations across the build plate. Another objective of this work is in understanding how porosity distributions and morphologies change with hot isostatic pressing, and, using FE analysis derive empirical relationships for the Young's modulus, [40]. These empirical relationships in conjunction with the non-destructive and fast ultrasound testing, will lead to future improvements of equipment, lasers and powders. Looking ahead, It may also be possible to use similar empirical

relationships for tensile and fatigue strength properties versus porosity - reducing the time taken to prepare and optimise a new material on a given powder bed process.

2 Materials and experimental procedure

2.1 Processing parameters and material specification

All components in this study were made using the powder bed laser fusion process of the Renishaw AM250 machine. This uses an Ytterbium fibre laser in Q-switched mode with a maximum power of 200 W and nominal laser spot diameter 70 µm. There are a wide range of parameters that can be varied in order to change the part properties and include but are not limited to, material specific parameters, laser parameters, scan parameters and environmental parameters.

The material used in the current investigation was the austenitic metastable 316L stainless steel powder with a nominal size range 15 to 45µm, spherical morphology manufactured via gas atomisation as shown **Figure 1 (a)**. The specification and actual composition (as supplied) of the alloy are shown in **Table 1**. Actual powder size distributions were D(10)=18.86 µm, D(50)=29.21 µm, D(90)=45.10µm. Both the powder morphology and particle size distributions have been shown to be important to the densification characteristics, and ultimately to the level of laser power which needs to be delivered at each layer [34], and to this extent the powder used in this study had similar characteristics.

A driving parameter of the densification of ALM parts is the Energy Density (E_d) [J/mm^3] is typically given by, [34]:

$$E_d = \frac{P_{laser}}{v_{scan} \cdot s_{Hatch} \cdot t_{Layer}} \tag{1}$$

However, as the laser on the AM250 is RF modulated, so the following relationship has been used:

$$E_d = \frac{Lower\ Power \times \left(\frac{exposure\ time}{hatch\ space\ \times point\ distance}\right)}{layer\ thickness} \tag{2}$$

In equation (2), the exposure time (ET), point distance (PD), hatch space (HS), layer thickness (LT) and power of the laser (P) are machine settings which define the laser energy density in the powder bed laser fusion process. The dimensions for the point distance, hatch space and the meander hatch pattern are shown in **Figure 1 (b)**. The nominal settings as recommended by the machine manufacturer for the specific 316L powder used were an exposure time of 110 µs, a point distance of 65 µm, a laser power 180 W, a layer thickness 50 µm and a 124µm hatching space.

For the density and elasticity part measurements cubes with 12mm sides were built in which the exposure time varying between 70-150 µs and the point distance varying between 25-105 µm over 3 levels, resulting in the 3X3 test parameter matrix given in **Table 2**. Each parameter combination was repeated three times giving a total of 27 cubic samples as shown in **Figure 2**. For each set of repeats, the laser energy density has been calculated using equation 2 giving laser energy densities ranging from a minimum of 19 J/mm^3 to a maximum of 175 J/mm^3, with the nominal settings corresponding to an input energy density of 49 J/mm^3. Line speeds are also given in **Table 2**, and range from 166 to 1500 mm/s, with the nominal line speed of 590 mm/s.

It is important to note that the exposure time and point distance ranges examined are much wider than are normally used for parameter optimisation, and this was done purposefully to create a wide range of resulting porosity over which to the effects of hot isostatic pressing could be examined.

Throughout the build process, the ambient temperature was maintained at 21˚C and O_2 levels within the chamber are minimised by combining a -960mbar Vacuum and back-filling to a +10mbar above atmospheric argon atmosphere resulting in O_2 below 100 ppm.

2.2 Tensile test specimen preparation

Two different specimen geometries and machines were used for the tensile tests, for which the sample geometries are shown in **Figure 3**. These specimens were manufactured using the nominal machine settings given in the previous section corresponding to a line speed of 590 mm/s and a laser energy density of 49.13 J/mm^3.

1) **42 Rectangular tensile bars** – These specimens were built net-shape with a 3 mm thickness, a 40 mm gauge section and a 100 mm total length, as shown **Figure 3 (a)**. This specimen geometry complies with the suggested sizes specified by the ASTM Additive Manufacturing standards committee (ASTM-F42) which has adopted ASTM E8 sub-specimen standard for metals, [41]. It also complies with the BS EN ISO 6892-1:2009 specimen dimension, [42]. A preliminary set of 42 test bars were built directly from the CAD in various orientations to the wiper (0°, 45° and 90°) on the build plate, and in a vertical (V), horizontal (H) and at 50° direction to the vertical (V50°) as shown in **Figure 4** , requiring a variety of support structures. 21 of these specimens underwent the HIP cycle described in the next section.

2) **6 Cylindrical tensile bars** – In the same build, 3 cylindrical rods were built vertically (100mm long and with a diameter of 20mm) with 1 rod undergoing the HIP cycle defined in the next section. Each rod was cut in half, each machined to 10mm diameter, with a 10mm long thread added to each end and then machined to a 5.65mm diameter along the 25mm gauge length. This yielded a total of 6 specimens (4 as-built and 2 hot isostatically pressed), as shown **Figure 3 (b)**. The geometry for these specimens complied to ASTM E8 sub-specimen standard, [41].

2.3 Hot isostatic pressing

The hot isostatic pressing cycle was done at TTI Groups' HIP facility in Letchworth, United Kingdom. The entire cycle lasted about 14 hours, with the samples (tensile test bars and cubes) heated to a temperature of 1125°C for 4 hours at 137MPa. The soak temperature was reached in 17 hours, and then allowed to furnace cool for 6 hours. For reference, the nine cubes which were hot isostatically pressed (A1-1, C1-1, C2-2, A3-1, A2-2, B3-2, C3-3, B2-2) were measured for density using the Archimedes' based methods prior to being hot isostatically pressed, and re-labelled (A1-1H, C1-1H, C2-2H, A3-1H, A2-2H, B3-2H, C3-3H, B2-2H) for post-HIP density measurement and microscopy analysis of porosity.

2.4 Metallographic preparation of sectioned cubes

The cubes underwent a series metallographic preparation routes depending on the analysis requirement, including optical images of grain structure and porosity, scanning electron microscope images of porosity and compositional Energy Dispersive X-ray (EDX) Analysis and polished surfaces for ultrasound testing. In all cases, to ensure that the surfaces were a representation of the bulk

material, approximately 1mm of material was removed by grinding the surface using a coarse grade SiC P240 paper, using a micrometer before and after polishing to ensure that at least 1 mm of material was removed during polishing.

Samples were prepared using standard metallographic techniques and etched to reveal the grain structure, after fine polishing the samples were etched in a solution (100 mL ethanol, 100 mL HCl, 5 g CuCl$_2$) for 7-9 minutes. SEM samples were mounted in conductive bakelite.

Some preliminary low magnification images of the cubes with little or no metallographic preparation are shown in **Figure 5**. Individual melt pool tracks traversing in a meander hatch pattern can be distinguished in **Figure 5 (a), (b), (c) and (e)**. Note the poorer track consolidation for (a) sample C1-3 and (d) C1-2, in which powder particles can be seen in the voids. **Figure 5 (f)** shows sample A1-3 from the side, and semi-sintered powder can be seen still attached to the sample.

2.5   Gravimetric measurements of bulk density

The three methods to calculate bulk density by gravimetric methods were:

  a. Callipers used to get approximate dimensions and volume divided by weight
  b. Archimedes principle weighing in and out of distilled water with a modified weighing scale
  c. Archimedes principle using a tensiometer Attension Sigma 700/701

The results of these measurements are given in **Table 3**. Published values of the theoretical density of 316L steel range from 7.95 g/cm^3 [43] to 8.00 g/cm^3, so for the relative density a value of 7.99 g/cm^3 was used which matches previous work [44]. In the water immersion tests, lacquer was applied to the cubes to minimise ingress into open porosity at the surface of the sample for the more porous samples.

2.6   Optical image analysis to determine porosity levels

Optical microscope images were used to observe and quantify the porosity of selected polished samples, for as-built and hot isostatically pressed cubes. For each cube, five different locations on the sample cross-sections were imaged at about 100X magnification, giving an area coverage of 20% of the sample, and sufficient pixel resolution to establish porosity down to 2-5μm.

Image analysis was undertaken on these images using the ImageJ software to quantify the level of porosity of the cubes. This was done by adjusting the brightness threshold of the image, and converting them to a black and white binary. In some instances the images were de-speckled and smoothed to reduce the occurrence of artificial porosity identification. The porous area fraction can then be calculated automatically on the basis of the contrast between dark porosity and light solid material.

2.7   Elasticity measurements using ultrasound

Sound velocity measurements were made using an Olympus D38 pulse echo precision thickness gauge, with two transducers, one for the longitudinal wave (10 MHz broadband longitudinal transducer) and the other for the shear modes (5 MHz normal incidence shear wave transducer).

The cube samples tested with ultrasound were in the as-built and hot isostatically pressed conditions, as described in section 2.1. Opposite faces were ground and fine polished, as described

in section 2.4, to ensure a good ultrasound signal was transmitted into the wall and reflected off the opposite surface. The accuracy of the depth gauge was benchmarked against two mild steel plates of 6mm and 10mm thickness. Subsequently, the distances between cube faces being sampled was measured using callipers, and then the transducer was applied to one surface, with appropriate specialised ultrasonic coupling fluids (glycol and high viscosity shear gel) applied to the sample face, for each of the longitudinal and shear velocity tests. The gauge returns sound velocity based on:

$$Velocity\ (m/s) = \frac{Thickness\ (m)}{0.5\ X\ Round\ trip\ transity\ time\ (s)}$$
(3)

According to the ASTM Standard Practice 494 for Measuring Ultrasonic Velocity in Materials,[45] the formula to calculate Poisson's ratio from the longitudinal and shear velocity values:

$$Poisson's\ Ratio\ (\nu) = \frac{1 - 2\left(\frac{V_T}{V_L}\right)^2}{2 - 2\left(\frac{V_T}{V_L}\right)^2}$$
(4)

Where, $V_T = Shear\ (traverse)\ velocity$, and $V_L = Longitudinal\ velocity$ of sound, both in metres per second (m/s).

Using these values in conjunction with a measured density, it is possible to calculate the effective Young's modulus (GPa) from:

$$Young's\ Modulus\ (E) = \frac{V_L{}^2 \rho (1+\nu)(1-2\nu)}{1-\nu}$$
(5)

Where $\rho = density$ (kg/m^3). Finally, the shear modulus can be obtained by using the following expression:

$$Shear\ Modulus\ (G) = V_T \rho$$
(6)

3   Results

3.1   Bulk density and porosity measurements

The average of the bulk density as measured using the gravimetric methods described in section 2.5 are given for both the as-built and hot isostatically pressed samples in Table 3. The average is a result of a minimum of three repetitions using each of the three gravimetric methods. This was used to calculate the relative density which using the gravimetric analysis gave values ranges from 77% to 98% for the as-built samples with up to 1.48% standard deviation, and from 80% to 99% for the hot isostatically pressed with up to 2% standard deviation. For one particular sample (C11) inter-connected porosity was visible by eye, leading to water ingress even with the lacquer coating. This was clearly captured by the tensiometer which is sensitive enough to capture changes in forces arising from surface tension as the sample is immersed in the test fluid.

Also given in the same table are calculated relative densities from the optical porosity measurements for comparison, which give values of relative density ranging from 59.5% to 99.64% for the as-built samples, with a 8.44% standard deviation and 87% to 100% with a 3% standard deviation for the hot isostatically pressed samples. The measured values and averages of the image-based measurements are given in **Table 4.**

7

Shown in **Figure 6** is the relative density as measured by the different methods plotted against laser energy density, including the relative density estimated from the optical measurements. The data follows a clear trend with the least dense samples corresponding to the lowest laser energy density samples, followed by a steep rise in density to an optimal density which falls in in the range of 49-79 J/mm^3 laser energy densities.

Comparing the methods of density measurement, a couple of aspects stand out. The optical measured values of porosity have higher levels of standard deviation than the gravimetric measurements, but generally lower values than the porosity derived from the gravimetric tests. The accuracy of the optical method for measuring porosity is directly related to the total area covered by the micrographs, which in the current work only accounted for 30-40% of the entire sample cross-section (144 mm^2). On the other hand, the gravimetric methods have a lower standard deviation for the less dense samples.

The average relative density across all measurements techniques is compared between the as-built samples and the hot isostatically pressed samples in **Figure 7**. As can be seen, the same trend occurs for both sets of samples in that the relative density increases with laser energy density up to a certain optimal level and then decreases. For the as-built samples this optimal energy density occurs in the 60-81.29 J/mm^3 range, whilst for the hot isostatically pressed samples it is in the 49-60 J/mm^3 range. After this the relative density of the as-built samples starts to decrease with higher laser energy density, whereas for the hot isostatically pressed samples the relative density remains relatively constant at 98.89%.

3.2   Microstructural characterisation and porosity morphology

The trends in relative density are corroborated and better understood by looking at the optical micrographs showing the porosity in **Figure 8**. What should be noted, is that for the as-built samples in **Figure 8** (a-f), there is a transition between a jagged more angular porosity at the lower laser energy density, which clearly shows incomplete laser coverage of the layer, through to overall lower levels of porosity at an optimal laser energy density (sample A1-2 with 81.29 J/mm^3). At this point the trend is reversed and an increasing level of more rounded/circular porosity evolves with increasing laser energy density beyond 81.29 J/mm^3.

This reversal of the densification trend with laser energy density for 316L has been seen before, see for example Kamath et al [46], and is even more apparent at higher laser power of 400W. Possible causes such as a transition to keyholing are examined in more detail in the discussion section.

What can also be seen from **Figure 8** (g-l) is that the hot isostatic pressing process is highly effective at closing the porosity, especially the more rounded porosity which appears to have completely closed at the higher laser energy density input.

Shown in **Figure 9**, are the porosity micrographs laid out in a matrix giving an overview of the effect of the variance of the point distance along the columns (A - 25 µm, B - 65 µm, C - 105 µm) and the exposure time along the rows (1 - 70 µs, 2 - 110 µs, 3 - 150 µs). This clearly shows that the larger point distance has the greatest contribution to the lack of proper coverage whereas the increasing exposure time widens the melt tracks, but is also strongly involved in the formation of the more rounded porosity (e.g. A3-1) associated with high laser energy densities.

The Feret diameter, also called the calliper diameter, is the distance between the two parallel planes restricting the particle (or pore) to that direction. The circularity index (0-100%) of the pore is taken as:

$$Circularity\ (\%) = 4\pi \frac{A}{P^2} \tag{7}$$

Where, P is the perimeter (µm) and A is the area of the pore (µm^2). Both the Feret diameter and the circularity are prone to higher levels of error in the smaller pore size ranges (<5µm) due to microscope magnification, pixel sizes and metallographic preparation.

The distributions of Feret diameters of pore sizes for as-built samples are shown in **Figure 11** and for the hot isostatically pressed samples are shown in **Figure 12**. Both distributions quantify what can clearly be seen from in **Figure 9**, namely that the whilst 30-40% of the pores have Feret diameters below 20µm, it is the C1 to C3 samples with the high point distances which have significant number of pore diameters in larger size fractions. When comparing the distributions of the as-built to the hot isostatically pressed samples it can be seen that the hot isostatic pressing is shifts the distributions towards the sub 20µm range, as well as lowering the number of larger pores sizes, as would be expected and visible in **Figure 9**. Plotting the maximum Feret diameter of the pores as a function of the laser energy density in **Figure 13** shows the significant reduction in maximum pore sizes which results from the hot isostatic pressing.

Average distributions of circularity of the porosity are shown in **Figure 14** for the number of pores in a given circularity band, where averages have been taken across all as-built and hot isostatically pressed samples. In comparison with the pore Feret diameters, circularity is not readily identifiable visible from the micrographs in **Figure 8** and **Figure 9**. There is a narrower distribution in the higher circularity bands for the as-built samples, whereas the hot isostatic pressing makes for a broader distribution with a lower circularity index. This is counter intuitive as common understanding would suggest that hot isostatic pressing would close and make all pores more rounded. These results should be taken lightly as in the smaller porosity bands there are up to 40% of pores with circularities above 100%, an artefact of image pixel resolution. However, if this result is accepted a possible explanation is that deformation during hot isostatic pressing is itself affected by the directionality of the porosity occurring along adjacent melt tracks hence the porosity is preferentially closed in a direction perpendicular to the track, resulting in final smaller porosities with higher aspect ratios.

Scanning Electron Microscope (SEM) images in **Figure 15** show typical morphologies of the pores. **Figure 15 (a) and Figure 15 (b)** show large pores (>200µm) due to incomplete track coverage with unmelted semi-sintered spherical powder particles still in the voids for the C1-2 sample (low energy density of 19.36 J/mm^3). More complete track coverage of the surface is seen in sample B2-3 (medium-low energy density of 49.13 J/mm^3), with smaller, angular 25-50µm pores which seem to be left at the junctions of tracks, as shown **Figure 15 (c) and (d).** The types of pores found in A1-2 (optimal laser energy density of 81.29 J/mm^3) are rounded and much smaller 10-25µm, as shown **Figure 15 (e) and (f).** Finally, the pores found in the sample A3-2 (high energy density of 174.19 J/mm^3 are shallow, rounded, but slightly larger (up to 100µm) and more frequent, as seen in **Figure 15 (g) and (h)**. Unlike pores in the other samples, the porosity in A3-2 shows no un-melted particles or junction-type pores, but there appear what look like tide lines within the void.

Etched microstructures are shown in **Figure 16** specifically for two samples with an equivalent level of laser input in the as-built (B23) and hot isostatically pressed (B22) conditions. At the higher magnification, the as-built sample reveals a convoluted microstructure with smaller less- well defined grain boundaries, consistent with the higher cooling rates expected from the melt pool solidification. Also, there is evidence of micron or sub-micron inter-grain cellular structures suggesting columnar growth in the build direction (out of plane direction) (see also **Figure 15 (f)**). According to [47], these cellular columnar growths also occur in cast and welded 316L but with much larger crystal columns 30-40μm, related to the cooling rates. A number of different formation mechanisms including compositional driven mechanisms due to supercooling, interfacial instabilities and Maragonni convection, but none of these have yet been proved.

In comparison, the hot isostatically pressed images, shown in **Figure 16 (d-f),** show a more homogeneous microstructure with larger grains and sharply defined grain boundaries. Also, in **Figure 16 (d) and (e), a**nnealing twins can clearly be seen between grains in the hot isostatically pressed microstructure, which is known to occur during re-crystallisation of austenitic steels , see [48], [49]. Both these features are consistent with the lower cooling rates of the HIP cycle.

There is also possible evidence of sensitization in the hot isostatically pressed samples, in **Figure 16 (d),** which is a precipitation of chromium carbides from the annealing twins to the austenitic grain boundaries, [50]. This is sometimes linked to improper heat treatment as 316L stainless steels are often chosen for corrosion resistance and rely on chromium to reduce corrosion, and sensitization leads to areas of locally depleted chromium which in turn leads to corrosion along grain boundaries. The sensitization can be removed by heat treating to 980°C and rapidly cooling to dissolve the carbides in the austenite.

Further analysis is required on the samples to determine levels of ferrite and austenite using XRD, EBSD, as these strongly determine the yield strength and ductility achievable for 316L.

3.3   Tensile test results

Tensile tests were performed on two different machines. The rectangular cross-section test bars, **Figure 3 (a)**, were tested in the Materials Research Centre on a Hounsfield universal testing machine with a 25kN load cell, and an extensometer measuring up to 12.5mm elongation. The circular cross-section specimens, **Figure 3 (b)**, were tested on a UKAS calibrated ESH 100kN universal testing machine with hydraulic wedge grips under stroke control and a 25mm extensometer. In both cases, the strain rate was set at 1 mm/min.

As an example of the results for the rectangular cross section test bars, engineering stress-strain curves are shown in **Figure 17** for the bars built at 50° to the vertical, the as-built yield stress is about 475-520MPa with a UTS of 500-550MPa, whereas for the hot isostatically pressed specimens the YS comes down to 250MPa with the lowered UTS ranging of 530-600MPa. The elongation of the as-built samples ranges from 1-8%, which increases to 37-47% for the hot isostatically pressed samples.

Stress-strain curves for the circular cross-section bars, for both the as-built and hot isostatically pressed test bars are shown in **Figure 18.** In this case, the results show greater strength and ductility for both the as-built and hot isostatically pressed samples. For the as-built specimens the YS ranges from 510-540MPa, the UTS ranges from 550-600MPa and the elongation falls between 5-14%. For the hot isostatically pressed samples the YS are lower at about 270MPa and the UTS are higher at

600MPa, with elongation ranging from 50-60%. The stress-strain curves have been compared directly to those of Malloy et al [51], which show very similar YS, UTS and elongation values for non-irradiated room temperature tensile tests.

When comparing the stress-strain curves and tensile properties for the cylindrical and rectangular test bars, it is clear that the cylindrical test samples give much better material properties, with higher UTS, YS and elongations much closer to properties of 316L plate and wrought materials, [32], [52]. This improvement when using machined samples is well known to give results more representative of the bulk material, stemming from the removal of the skin layer from which cracks can initiate.

The stress-strain curves are not shown for all 42 rectangular cross-sectioned samples, but rather the YS and UTS averages are summarised from 3 samples in each of three orientations to the wiper and 3 orientations to the vertical, for both as-built and hot isostatically pressed samples, as shown in **Figure 19**. Across all build orientations, hot isostatic pressing increases the average UTS from 524MPa to 542MPa and lowers the standard deviation from 68MPa to 48MPa. Hot isostatic pressing lowers the YS from an average of 385MPa to 227MPa, but generally homogenises the YS across all build directions and orientations with a standard deviation of 5MPa.

For all the vertically built samples, the average UTS in as-built condition is 469MPa with a standard deviation of 72MPa, and the average UTS of hot isostatically pressed samples is 513MPa with a standard deviation of 49 MPa. For all the horizontally built samples, the average UTS in the as-built condition is 577MPa with a standard deviation of 13 MPa and the average UTS when hot isostatically pressed is 566MPa with a standard deviation of 9MPa.

In terms of the orientation to the wiper, there is no clear pattern to the results within the overall levels of deviation, but generally the parts built with sides either parallel or at right angles to the wiper are stronger than those built at 45°.

The average elongation across all hot isostatic pressed samples is 40.89% with a standard deviation of 9%, which is a significant increase over the as-built sample average of 21.83% with a standard deviation of 12.4%, as shown in **Figure 20**. However, there is a significant difference between the horizontally built samples and those built vertically. Even the hot isostatically pressed samples have a significantly lower elongation (28-29%) for the vertically built samples, and a higher level of standard deviation.

The fracture surfaces of rectangular specimens are shown in **Figure 21**, for horizontally as-built specimen, **Figure 21 (a)**, a vertically as-built specimen, **Figure 21 (b)**, a horizontally built hot isostatically pressed sample, **Figure 21 (c)**, and for a vertically built hot isostatically pressed sample, **Figure 21 (d)**. Note the presence of a surrounding skin layer on which can be seen sintered powder particles as the rectangular samples received no post-build machining treatment.

At a macro-scale, for the circular cross-section samples there was no evidence of the classic cup and cone fracture surface expected from ductile materials like 304 and 316L steels, [53], although for the rectangular as-built samples the fracture surfaces were generally flat and the hot isostatically pressed samples showed 45° fracture planes.

At a micro-level, there is evidence of dimple-like structures which would indicate local ductile behaviour, [30], [32] for both the as-built, see **Figure 22** and **Figure 24(a),** and the hot-isostatically pressed samples, see **Figure 23** and **Figure 24(b)**. A spherical dimple-like formation indicates microvoid formation prior to crack initiation. The as-built samples show a finer, more-jagged dimple structure, whereas in the hot isostatically pressed test bars a much clearer dimple formation is seen akin to that of wrought/hot rolled plate fractures, [52], albeit in both cases with smaller dimple sizes.

3.4 Elasticity measurements using ultrasound

The measured longitudinal and shear wave velocities for the range of as-built and hot isostatically pressed cube samples are given in **Table 5**, which together with the average measured density can be used to derive Poisson's ratio, the Young's modulus and the shear modulus. These are plotted as a function of laser input energy are shown in **Figure 25**, and can be seen to be closely related to the densification curves, as one would expect from the equations used (5 & 6). The highest measured Young's modulus for the as-built samples is 195.54 ±7.0 GPa, and the highest measured value for the hot isostatic pressed sample is 202.23 ±12.4 GPa. There is a clear increase in Young's modulus with hot isostatic pressing.

For cross-reference, the average Young's modulus obtained from the tensile stress-strain curves for the horizontally built bars was 139±47 GPa (as-built) and 179±72 GPa (hot isostatically pressed), and for the vertically built bars was 78±4 GPa (as-built) and 122±32 GPa (as-built). The ultrasound testing had significantly lower levels of standard deviation in the Young's modulus than the tensile tests, which is thought to be due to machine sensitivity. Other researchers have used tensile testing measurements to obtain Youngs modulus for 316L SLM samples, such as Mower et al, [20] who measured values in the 180-193 GPa range, and Zhang et al., [30] who measured values in the 151±13.1-194±14.5 GPa range.

The Poisson's ratio is plotted as a function of the laser energy density in **Figure 26** and although noisier than the elasticity moduli, at higher density values it generally falls in the range of published values. This is important, because unlike the elasticity moduli, it does not depend on the measured density of the sample, so is purely a function of the ultrasound measurements.

3.5 Empirical relationships and Finite Element Analysis

A comprehensive review of the relationships between Young's modulus and porosity is given by Choren et al, [40], specifically for the type of porosity arising from additive manufacturing processes. They conclude that the wide range of empirical formulations which have been developed for other processes (e.g. powder metallurgy or casting) are either based too much on theoretical pore morphology with an idealised microstructure or demonstrate too wide a disparity to be useful.

These empirical correlations typically take the form used by Chawla et al. [3], using a formulation derived by Ramakrishnan et al. (R–A), [54], which gives the effective Young's modulus of a material, E, with a given fraction of porosity, p, as:

$$E = E_0 \left[\frac{(1-p)^2}{1+\kappa_E p} \right] \tag{8}$$

12

Where, E_0 is the standard or nominal value of Young's modulus (210GPa) for 316L at room temperature. An alternative empirical relationship for E as a function of porosity is given by Roberts et al,[55]:

$$E = E_0 \left[1 - \frac{p}{0.5} \right]^{2.23} \tag{9}$$

Finite element (FE) analysis was also undertaken to derive effective Young's modulus and compare with measured and empirical correlations for the elasticity parameters, specifically as a function of porosity. The FE analysis allowed the relationship between the size, morphology and distributions of porosity to be better understood.

The FE stress analysis (ANSYS Mechanical Workbench 15) consisted of a transient elasto-plastic analysis in which a velocity of 1.667 mm/s was applied along a top boundary, whilst the lower boundary was kept fixed in all directions, as shown in **Figure 27**. For the elastic regime of the FE analysis, standard values of Young's modulus (210GPa), Shear modulus (77 MPa) and Poisson ratio (0.29) were used. A multilinear isotropic hardening curve was used to describe the non-linear plasticity regime based on the experimental data of Malloy et al., [51], with a yield strength value of 300 MPa to determine the onset of plasticity in the model.

Two types of geometry were analysed:

- The first type of geometry used arrays of regularly distributed pores (circular and rhomboidal) as shown in **Figure 28**, which shows typical Von Misses stress distributions on the deformed geometry. Shown in **Figure 29**, are a number of the FE meshes as an example of the pore arrangements examined. Also shown are elasto-plastic strain contours and contours of equivalent or Von-Misses stress for porosity formed for geometries with an increasing circular or rhomboidal porosities.
- The second type of geometry used pore distributions derived by digitizing porosity obtained from a micrograph (2.7mmX1.97mm) imported through CAD into ANSYS, and extruding it in the z-direction to create a 3D body. In both cases relatively fine meshes were used to capture the details of the porosity. This was done for two micrographs namely for sample A32 (4.18% rounded porosity) and for sample B13 (12.94% jagged porosity), and some of the results are shown in **Figure 31**.

The stress-displacement curves from the FE analysis are summarised in **Figure 32**, for all geometries. As can be seen there is a decrease in the yield stress and the effective Young's modulus as the porosity increases, whereby the effective yield stress goes from 300MPa at 0% porosity down to 75MPa at 44.2% porosity. The decrease in yield stress due to the sharper rhomboidal porosity (blue lines) is much more severe, with a drop to 75MPa at 30% porosity.

In the same graph are the stress-strain curves for porosities derived from micrographs. It should be noted that the more rounded micrograph (A32) with 4% porosity has a similar level of yield stress at about 230-250MPa as circular porosity at 7.1% and rhomboidal porosity at 2.5%. The micrograph B13 has a higher porosity level (12%) which is more angular and results in lower predicted yield strength of 160MPa, similar to the predicted yield strength for circular porosity at 15.9%, and rhomboidal porosity at 11%.

13

The effective Young's modulus is compared to the empirical, FE results and measured data values in **Figure 33**. This shows that the exponential trend of the empirical equations is matched by the FE simulations over a wide range. There is a clear distinction in the FE results between regular angular pore geometry (rhomboidal) and the circular porosity, with the sharper pores giving clearly higher stress concentrations and earlier failure.

The normalised Young's modulus (E/E_0) is plotted against the relative density over a smaller range of porosity in **Figure 34**, for the empirical, FE results and measured data values. What is clear is that the measured hot isostatically pressed samples are closer to the trends for the circular FE and empirical equations, and that the as-built samples lie below and are close to the angular FE and empirical equations.

4   Discussion

4.1   Discussion on the bulk density and porosity measurements

In this work, it has been shown that components made by powder bed laser fusion have a degree of porosity which is closely related to the level of laser energy used in building the component. An optimal set of machine parameter values exist (in this case laser point distance travel and laser exposure time), which, for the 316L steel powder studied here gives a minimum porosity of 2% in the as-built part. It should be pointed out that the machine parameters were varied over a wider range than is typically considered to get a good fundamental understanding of how they affect the build, and that in production, the machine would never be run at such extreme cases.

The porosity has been shown to be highly directional in nature at low levels of laser energy density less than 49 J/mm^3, and the resulting bulk porosity is much higher (up to 22%) and at the microstructural level, the porosity tends to follow the hatch pattern and build layers, with wide (>150µm), irregular-shaped, sometimes deep jagged pores, with evidence of un-melted powder particles inside the pores. The predominant porosity mechanism would appear to be from a lack of laser coverage, but may be also influenced to a lesser extent on balling/surface tension effects in the melt pool.

What is interesting is that while the optical micrographs of the densest parts which have been hot isostatically pressed suggest that the porosity is hardly visible (<0.1%), the gravimetric measurements suggest that the parts are not 100% dense. To this extent, a conclusion might be that there is remaining amount of very small, highly dispersed pores not captured at the used microscopic magnification, or that some of the Argon gas has become dissolved into the solid lowering the bulk density. A counter argument to this conclusion is that the current data is inconclusive due to the levels of measurement error is too high. Furthermore, the optical analysis was only carried out on horizontal surfaces of the samples i.e. in the plane of the build, although it is known that there are also significant differences in the porosity structure and distributions parallel to the build direction. Higher resolution and microscopy coverage would be needed to examine this further.

At the other extreme, at increasing laser energy densities higher than the optimal one of 49 J/mm^3, porosity re-appears in the as-built samples, but in this case the porosity is shallow and highly spherical in nature, and typically no bigger than 20-30µm diameter, with an overall porosity no higher than 2-3%. It is believed that this type of porosity may arise from keyholing as seen in laser

welding and more recently in powder bed laser fusion [46], [56], [57]– when temperatures in the melt-pool rise above the vaporisation temperature of the various alloy components and a plasma is formed, enhancing laser absorption. The plasma would absorb and re-emit laser radiation in such a way that it essentially can bore its way through sublayers, already previously solidified. When the keyhole solidifies, the entire keyhole is filled in with melt-pool and would probably only be evidenced by small dimples which are quickly filled over by the next layer of the build. The material within these dimples contain a level of entrapped argon or oxide films which upon metallographic preparation gives the spherical shaped porosity seen in the current work.

King et al, [56] have derived a criteria for the transition between conductive and keyhole melting which is based on the normalised enthalpy as

$$\frac{\Delta H}{h_s} = \frac{AP}{h_s\sqrt{\pi D u \sigma^3}} > 6 \tag{10}$$

Where, A is the absorptivity (for steel = 0.4), P is the laser power (W), h_s is the enthalpy at melting (1.2X10^6 J/kg), D is the thermal diffusivity (5.38X10^{-6} m^2/s), u is the beam velocity (m/s) and σ is the beam spot radius (m). The normalised enthalpy has been calculated for all the machine parameters used in this study and is given in Table 2 alongside the laser energy density. Based on this criterion, samples A2 and A3 with the high exposure times are close to the transition criteria, suggesting that a keyhole melting regime is possible.

Much effort is being made to understand the fundamental physics of powder melting at the micro-level, [58]–[61], and this includes the transition and formation of the keyhole melting regime, as it is generally accepted that this regime is best avoided to minimise detrimental effects on mechanical properties.

4.2   Discussion on the elasticity measurements using ultrasound

Published data on 316L wrought and rolled steel using ultrasound methods, see [62]–[65], have given Youngs moduli in the order of 195-196GPa, shear moduli in the 75.2-75.7 GPa and Poisson ratio in the order of 0.293-0.294, which are in pretty close agreement with the measured properties in the current work. Shankar et al [66] give values of Young's modulus as 196.79±0.41 GPa, shear modulus of 76.10±0.3 GPa and Poisson ratio of 0.293±0.001, and interestingly mention that microstructural variations arising from heat treatment can affect the properties, especially through the formation of chromium nitrides. It is interesting to note that the density in these publications is slightly lower at 7.79-7.97 g/cm^3 than that the 7.99 g/cm^3 used herein for the calculation of relative density. It is thought that small variations in the chromium and nickel content of the 316L alloy may be the cause of this difference, which would also imply that the .

Aside from Fischer et al, [67], for Ti-6Al-4V, and Stowinski et al., [68], for a Co-Cr alloy, no other publications were found in which ultrasound had been used to determine the elasticity properties of materials fabricated using powder bed processes.

This is surprising as the technique is relatively simple and high throughput giving rapid information on the elasticity properties of the as-fabricated and heat treated parts.

4.3   Discussion on the tensile test measurements

The tensile properties obtained in this work should be compared to results from other researchers who have examined the tensile properties of 316L steel using other powder bed fusion systems. Mower et al [20] used a DMLS EOS M270 (195W and 750 mm/s) laser to build test bars in horizontal and 45 degrees directions in a nitrogen gas environment giving a YS (496-473 MPa), UTS (717-680 MPa), E(180-193 GPa) and elongation at failure (28-30%) – no density given. Zhang et al, [30], use a SLM250 Realizer with a continuous Nd:YAG laser (100W and 300 mm/s), with densities in the 98-99.7% ranges, YS (), UTS (500-600 MPa), E (150-194 GPa) and as-built elongations in the 10% range. Carlton et al, [32], use a Concept laser M2 (100W and 222 mm/s) to produce tensile specimens with a range of densities from 83-98%, giving as-built YS (590 MPa±17), UTS (705 MPa±15) and elongations (44%±7), and annealed properties of YS (375 MPa±11), UTS (635 MPa±17) and an elongation of (51%±3).

The orientation of the test bars with respect to the build plate plays a significant role in the maximum tensile test properties. In common with Tolosa et al [69] **and** some of the authors given in Table 6, vertically built samples generally were found to have a lower tensile strength than horizontally built samples, and significantly higher levels of standard deviation, and highly variable levels of elongation. Hot isostatic pressing generally homogenised the strength, and reduced standard deviation, but less so for the vertical test bars.

When comparing the current work to 316L material originating from wrought, sheet or rolled plate, hot isostatically pressed stress-strain curves have been compared directly to those of Malloy et al [51], and show very similar YS, UTS and elongation values. The tensile properties obtained in this work have also been compared to 316L prepared from solution treated and hot rolled plate, such as that tested by Song et al, [52], who find YS (220-245 MPa), UTS (565-585 MPa) and elongations in the 61-64%. Carlton et al, [32], also test a wrought specimen and find a UTS 545MPa, YS of 245MPA and an elongation of 55%. Generally, YS and UTS are slightly lower in this work, but pretty similar for the hot isostatically pressed samples. However, the current results show elongation is 14-20% lower, and there is a higher level of standard deviation.

A comparison with previous work would not be complete without a reference to as-cast samples. The only available recent studies on the mechanical properties of 316L are from studies conducted by ITER in the extensive study on 316L and the equivalent castable alloy for the ITER shield modules or diverter cassettes, [70]–[72]. In fact, Busby et al, [71] state that cast 316L did not meet these requirements , but a modified casting alloy, namely CF-3M was needed to capture the very specific mechanical requirements needed, which included a minimum high temperature, irradiation resistance and fatigue. It should be pointed out that CF-3M has a slightly different composition with higher allowable N and Mn, and N is known to be a solid solution

The hot isostatically pressed results in the current work fall within the range of YS and UTS of cast 316L and CF-3M as given by [73] and the ASM handbook, [74], if with a slightly lower ductility. However, there are high levels of scatter for mechanical property data for 316L prepared by both casting and laser melted, so to this extent it is not possible to make any categorical comparisons between the two.

4.4   Discussion on the empirical and Finite Element Analysis

It has been possible to use the empirical and FEA analysis to fit the measured elasticity data (particularly Young's modulus) onto curves which could be used in future to predict the values. However the porosity ranges examined here (1%-40%) were much higher than would naturally occur in the daily running of the powder bed machine, where porosities in the 0.5 to 1.5% are more typical. Due to this only a relatively small number of samples were tested. As the next generation of machines become available and the variations of porosity and build quality are improved, a larger of samples can be tested to come up with a more definitive equation for the Young's modulus/porosity relationship.

As the Young's modulus in metals is directly related to the atomic bonding and fatigue crack growth is the accumulated breakage of inter-atomic bonds, [75], [76], thus the fatigue threshold is also proportional to Young's modulus. To this extent, the same Young's modulus/porosity relationship could be used as a high-throughput method to predict fatigue strength variations across the build.

4.5   Final remarks

In this work, comparison has been made of the mechanical properties for samples as-built with those treated by a post-build hot isostatic pressing cycle. The effect of hot isostatic pressing on the density of the cubes showed that hot isostatic pressing both closed the porosity and generally tried to make it more spherical. The highest rates of porosity reduction were on samples with porosity higher than 6%, typically those resulting at the extremes of low and high laser energy input. However, in the case of the latter, porosity was reduced to 1% after hot isostatic pressing, whilst the former remained at 17% porosity even after hot isostatic pressing. The sectioned SEM images show that in the high porosity cubes, the inter-laser hatching porosity had reduced in size, but still had relics of powder particles trapped within the voids.

Although it is possible in some applications to live with a level of porosity, it is accepted that the lowest level of porosity is required, and indeed in many applications, especially in aerospace, the tolerance of porosity is low. In casting, porosity is differentiated between micro- and macro-porosity (pores >100 μm), with macro-porosity affecting general tensile failure through localised stress concentrations, but micro-porosity has a strong influence in fatigue resistance [77] and is often manifested in reduced elasticity, i.e. lower Young's modulus.

At the current stage in the development of the powder fusion process, there has been a move to higher power lasers in 400-500W range, which coupled with other process improvements such as in-line monitoring is leading to higher levels of density. While increases in laser power allow higher line speeds and hence faster build times for components, there may be constraints on the efficiency of the melting based upon the conductive to keyhole melting mode transition. Variations in process can come from a number of sources, at the level of the metal powder/ laser interaction, obscuration of lasers and focussing lenses, segregation of powder size distributions, uniform deposition of powder layers and gas flow uniformity are all areas under intense scrutiny and development.

Having said that, it is particularly clear in looking at the range of results available for tensile properties of 316L, that a direct comparison between castings, wrought and powder fusion is not a particularly useful exercise. Depending on applications which are extremely broad powder bed

material properties can be better, equal to or worse than these other processes, with possibly a larger amount of scatter which can be reduced with an appropriately optimised heat treatment.

5   Conclusions

To summarise, a number of general trends have been seen for 316L manufactured by a powder bed laser fusion process, which match other workers in that:

- Two distinct types of porosity are formed as the laser energy input is increased, but the overall as-built porosity can be below 1-2% at the optimal laser energy input;
- Hot isostatic pressing is able to reduce the porosity to below 1%;
- Hot isostatic pressing marginally increases the peak UTS values and lowers the standard deviation;
- Hot isostatic pressing significantly reduces the yield strength but increases the elongation, in both cases lowering standard deviation;
- Upper tensile strength is higher for horizontally built samples, than for vertically built samples;
- After hot isostatic pressing, there is still a 100MPa difference in UTS between samples built in vertical and horizontal directions;
- Improvements in ductility are reflected in the fracture surfaces of the hot isostatically pressed samples;
- Relationships between porosity and elasticity properties, such as Young's modulus have been examined through ultrasound measurements and are also directly related to the laser energy input
- The relationship between porosity and effective Young's modulus has also been examined through the use of finite element micro-models, and the results indicate that there is a similarity with empirical equations used for sintered parts

Further work needs to be done to understand:

- The root cause of the occurrence of porosity at high input laser energy for the densification of the parts which may be singular to 316L.
- Whether the standard hot isostatic cycle used was in effect the optimal cycle for 316L parts built by this particular powder bed laser fusion process.
- The relationship in as-built and hot isostatically pressed parts between porosity, elasticity and fatigue properties.

Acknowledgements

6   References

[1]   L. E. Murr, S. M. Gaytan, D. a. Ramirez, E. Martinez, J. Hernandez, K. N. Amato, P. W. Shindo, F. R. Medina, and R. B. Wicker, "Metal Fabrication by Additive Manufacturing Using Laser and Electron Beam Melting Technologies," *J. Mater. Sci. Technol.*, vol. 28, no. 1, pp. 1–14, 2012.

[2]   N. Guo and M. C. Leu, "Additive manufacturing: Technology, applications and research needs," *Front. Mech. Eng.*, vol. 8, no. 3, pp. 215–243, 2013.

[3]   N. Chawla and X. Deng, "Microstructure and mechanical behavior of porous sintered steels," *Mater. Sci. Eng. A*, vol. 390, no. 1–2, pp. 98–112, 2005.

[4]   K. Zhang, J. Mei, N. Wain, and X. Wu, "Effect of hot-isostatic-pressing parameters on the microstructure and properties of powder Ti-6Al-4V hot-isostatically-pressed samples," *Metall. Mater. Trans. A Phys. Metall. Mater. Sci.*, vol. 41, no. 4, pp. 1033–1045, 2010.

[5]   R. Lapovok, D. Tomus, and B. C. Muddle, "Low-temperature compaction of Ti-6Al-4V powder using equal channel angular extrusion with back pressure," *Mater. Sci. Eng. A*, vol. 490, no. 1–2, pp. 171–180, 2008.

[6]   Kuang J.P., Harding R.A., and Campbell J., "Microstructures and mechanical properties of an investment cast gamma titanium aluminide," *Mater. Sci. Tech.*, vol. 15, no. May, pp. 840–850, 1999.

[7]   C. Qiu, N. J. E. Adkins, and M. M. Attallah, "Microstructure and tensile properties of selectively laser-melted and of HIPed laser-melted Ti-6Al-4V," *Mater. Sci. Eng. A*, vol. 578, pp. 230–239, 2013.

[8]   E. Brandl, F. Palm, V. Michailov, B. Viehweger, and C. Leyens, "Mechanical properties of additive manufactured titanium (Ti-6Al-4V) blocks deposited by a solid-state laser and wire," *Mater. Des.*, vol. 32, no. 10, pp. 4665–4675, 2011.

[9]   N. Hrabe and T. Quinn, "Effects of processing on microstructure and mechanical properties of a titanium alloy (Ti-6Al-4V) fabricated using electron beam melting (EBM), part 1: Distance from build plate and part size," *Mater. Sci. Eng. A*, vol. 573, pp. 264–270, 2013.

[10]   S. Rawal, J. Brantley, and N. Karabudak, "Additive manufacturing of Ti-6Al-4V alloy components for spacecraft applications," *RAST 2013 - Proc. 6th Int. Conf. Recent Adv. Sp. Technol.*, pp. 5–11, 2013.

[11]   C. de Formanoir, S. Michotte, O. Rigo, L. Germain, and S. Godet, "Electron beam melted Ti-6Al-4V: Microstructure, texture and mechanical behavior of the as-built and heat-treated material," *Mater. Sci. Eng. A*, vol. 652, pp. 105–119, 2016.

[12]   M. Simonelli, Y. Y. Tse, and C. Tuck, "Effect of the build orientation on the mechanical properties and fracture modes of SLM Ti-6Al-4V," *Mater. Sci. Eng. A*, vol. 616, pp. 1–11, 2014.

[13]   A. B. Spierings, T. L. Starr, and K. Wegener, "Fatigue performance of additive manufactured metallic parts," *Rapid Prototyp. J.*, vol. 19, no. 2, pp. 88–94, 2013.

[14]   E. Chlebus, K. Gruber, B. Kuźnicka, J. Kurzac, and T. Kurzynowski, "Effect of heat treatment on microstructure and mechanical properties of Inconel 718 processed by selective laser melting," *Mater. Sci. Eng. A*, vol. 639, pp. 647–655, 2015.

[15] D. Zhang, W. Niu, X. Cao, and Z. Liu, "Effect of standard heat treatment on the microstructure and mechanical properties of selective laser melting manufactured Inconel 718 superalloy," *Mater. Sci. Eng. A*, vol. 644, no. 1–2, pp. 32–40, 2015.

[16] K. N. Amato, S. M. Gaytan, L. E. Murr, E. Martinez, P. W. Shindo, J. Hernandez, S. Collins, and F. Medina, "Microstructures and mechanical behavior of Inconel 718 fabricated by selective laser melting," *Acta Mater.*, vol. 60, no. 5, pp. 2229–2239, 2012.

[17] T. Vilaro, C. Colin, J. D. Bartout, L. Nazé, and M. Sennour, "Microstructural and mechanical approaches of the selective laser melting process applied to a nickel-base superalloy," *Mater. Sci. Eng. A*, vol. 534, pp. 446–451, 2012.

[18] W. Li, S. Li, J. Liu, A. Zhang, Y. Zhou, Q. Wei, C. Yan, and Y. Shi, "Effect of heat treatment on AlSi10Mg alloy fabricated by selective laser melting: Microstructure evolution, mechanical properties and fracture mechanism," *Mater. Sci. Eng. A*, vol. 663, pp. 116–125, 2016.

[19] K. Kempen, L. Thijs, J. Van Humbeeck, and J.-P. Kruth, "Mechanical Properties of AlSi10Mg Produced by Selective Laser Melting," *Phys. Procedia*, vol. 39, pp. 439–446, 2012.

[20] T. M. Mower and M. J. Long, "Mechanical behavior of additive manufactured, powder-bed laser-fused materials," *Mater. Sci. Eng. A*, vol. 651, pp. 198–213, 2016.

[21] N. T. Aboulkhair, I. Maskery, C. Tuck, I. Ashcroft, and N. M. Everitt, "The microstructure and mechanical properties of selectively laser melted AlSi10Mg: the effect of a conventional T6-like heat treatment," *Mater. Sci. Eng. A*, vol. 667, pp. 139–146, 2016.

[22] E. Brandl, U. Heckenberger, V. Holzinger, and D. Buchbinder, "Additive manufactured AlSi10Mg samples using Selective Laser Melting (SLM): Microstructure, high cycle fatigue, and fracture behavior," *Mater. Des.*, vol. 34, pp. 159–169, 2012.

[23] K. G. Prashanth, S. Scudino, H. J. Klauss, K. B. Surreddi, L. Löber, Z. Wang, A. K. Chaubey, U. Kühn, and J. Eckert, "Microstructure and mechanical properties of Al-12Si produced by selective laser melting: Effect of heat treatment," *Mater. Sci. Eng. A*, vol. 590, pp. 153–160, Jan. 2014.

[24] K. Bartkowiak, S. Ullrich, T. Frick, and M. Schmidt, "New developments of laser processing aluminium alloys via additive manufacturing technique," *Phys. Procedia*, vol. 12, no. PART 1, pp. 393–401, 2011.

[25] K. Schmidtke, F. Palm, a. Hawkins, and C. Emmelmann, "Process and mechanical properties: Applicability of a scandium modified Al-alloy for laser additive manufacturing," *Phys. Procedia*, vol. 12, no. PART 1, pp. 369–374, 2011.

[26] A. J. Sterling, B. Torries, N. Shamsaei, S. M. Thompson, and D. W. Seely, "Fatigue behavior and failure mechanisms of direct laser deposited Ti-6Al-4V," *Mater. Sci. Eng. A*, vol. 655, pp. 100–112, 2016.

[27] S. Leuders, M. Thöne, A. Riemer, T. Niendorf, T. Tröster, H. A. Richard, and H. J. Maier, "On the mechanical behaviour of titanium alloy TiAl6V4 manufactured by selective laser melting: Fatigue resistance and crack growth performance," *Int. J. Fatigue*, vol. 48, pp. 300–307, Mar. 2013.

[28] M. Akita, Y. Uematsu, T. Kakiuchi, M. Nakajima, and R. Kawaguchi, "Defect-dominated fatigue behavior in type 630 stainless steel fabricated by selective laser melting," *Mater. Sci. Eng. A*, vol. 666, pp. 19–26, 2016.

[29]   K. Guan, Z. Wang, M. Gao, X. Li, and X. Zeng, "Effects of processing parameters on tensile properties of selective laser melted 304 stainless steel," *Mater. Des.*, vol. 50, pp. 581–586, 2013.

[30]   B. Zhang, L. Dembinski, and C. Coddet, "The study of the laser parameters and environment variables effect on mechanical properties of high compact parts elaborated by selective laser melting 316L powder," *Mater. Sci. Eng. A*, vol. 584, pp. 21–31, 2013.

[31]   E. Yasa and J. P. Kruth, "Microstructural investigation of selective laser melting 316L stainless steel parts exposed to laser re-melting," *Procedia Eng.*, vol. 19, pp. 389–395, 2011.

[32]   H. D. Carlton, A. Haboub, G. F. Gallegos, D. Y. Parkinson, and A. A. MacDowell, "Damage evolution and failure mechanisms in additively manufactured stainless steel," *Mater. Sci. Eng. A*, vol. 651, pp. 406–414, 2016.

[33]   A. Yadollahi, N. Shamsaei, S. M. Thompson, and D. W. Seely, "Effects of process time interval and heat treatment on the mechanical and microstructural properties of direct laser deposited 316L stainless steel," *Mater. Sci. Eng. A*, vol. 644, pp. 171–183, 2015.

[34]   A. B. Spierings, N. Herres, and G. Levy, "Influence of the particle size distribution on surface quality and mechanical properties in AM steel parts," *Rapid Prototyp. J.*, vol. 17, no. 3, pp. 195–202, 2011.

[35]   R. Morgan, C. J. Sutcliffe, and W. O'Neill, "Density analysis of direct metal laser re-melted 316L stainless steel cubic primitives," *J. Mater. Sci.*, vol. 39, no. 4, pp. 1195–1205, 2004.

[36]   G. Miranda, S. Faria, F. Bartolomeu, E. Pinto, S. Madeira, A. Mateus, P. Carreira, N. Alves, F. S. Silva, and O. Carvalho, "Predictive models for physical and mechanical properties of 316L stainless steel produced by selective laser melting," *Mater. Sci. Eng. A*, vol. 657, pp. 43–56, 2016.

[37]   L. Löber, C. Flache, R. Petters, U. Kühn, and J. Eckert, "Comparison of different post processing technologies for SLM generated 316l steel parts," *Rapid Prototyp. J.*, vol. 19, no. January 2012, pp. 173–179, 2013.

[38]   N. Kurgan, "Effect of porosity and density on the mechanical and microstructural properties of sintered 316L stainless steel implant materials," *Mater. Des.*, vol. 55, pp. 235–241, 2014.

[39]   K. Kempen, E. Yasa, L. Thijs, J. P. Kruth, and J. Van Humbeeck, "Microstructure and mechanical properties of selective laser melted 18Ni-300 steel," *Phys. Procedia*, vol. 12, no. PART 1, pp. 255–263, 2011.

[40]   J. A. Choren, S. M. Heinrich, and M. B. Silver-Thorn, "Young's modulus and volume porosity relationships for additive manufacturing applications," *J. Mater. Sci.*, vol. 48, no. 15, pp. 5103–5112, 2013.

[41]   American Society for Testing and Materials, "E8/E8M – 09: Standard Test Methods for Tension Testing of Metallic Materials 1," *ASTM E8/E8M – 09*, no. C, pp. 1–27, 2009.

[42]   BRITISH STANDARDS, "BS EN ISO 6892-1:2009: Metallic materials - Tensile testing, Part 1 : Method of test at ambient temperature," *Met. Mater. - Tensile testing, Part 1 Method test Ambient Temp.*, 2009.

[43]   K. C. Mills, *Recommended values of thermophysical properties for selected commercial alloys*. Woodhead Publishing Limited, 2002, 2002.

[44]   J. a. Cherry, H. M. Davies, S. Mehmood, N. P. Lavery, S. G. R. Brown, and J. Sienz, "Investigation into the effect of process parameters on microstructural and physical properties of 316L stainless steel parts by selective laser melting," *Int. J. Adv. Manuf. Technol.*, vol. 76, no. 5–8, pp. 869–879, 2015.

[45]   American Society for Testing and Materials, "ASTM E494-95: Practice for measuring ultrasonic velocity in materials," *ASTM E494-95*, vol. 4, p. American Society for Testing and Materials, West C, 2001.

[46]   C. Kamath, B. El-Dasher, G. F. Gallegos, W. E. King, and A. Sisto, "Density of additively-manufactured, 316L SS parts using laser powder-bed fusion at powers up to 400 W," Livermore, CA, 2013.

[47]   K. Saeidi, "Kamran Saeidi Doctoral Thesis 2016," Stockholm University, 2016.

[48]   Y. Jin, M. Bernacki, G. . Roher, a. D. Rollett, B. Lin, and N. Bozzolo, "Formation of annealing twins during recrystallization and grain growth in 304L austenitic stainless steel," *Mater. Sci. …*, no. 753, pp. 113–116, 2013.

[49]   G. Sundararajan, P. S. Phani, a. Jyothirmayi, and R. C. Gundakaram, "The influence of heat treatment on the microstructural, mechanical and corrosion behaviour of cold sprayed SS 316L coatings," *J. Mater. Sci.*, vol. 44, no. 9, pp. 2320–2326, 2009.

[50]   J. M. Radzikowska, *Metallographer's Guide Practices and Procedures for Irons and Steels*. 2004.

[51]   S. A. Maloy, M. R. James, G. Willcutt, W. F. Sommer, M. Sokolov, L. L. Snead, M. L. Hamilton, and F. Garner, "The mechanical properties of 316L/304L stainless steels, Alloy 718 and Mod 9Cr-1Mo after irradiation in a spallation environment," *J. Nucl. Mater.*, vol. 296, no. 1–3, pp. 119–128, 2001.

[52]   R. Song, J. Xiang, and D. Hou, "Characteristics of Mechanical Properties and Microstructure for 316L Austenitic Stainless Steel," *J. Iron Steel Res. Int.*, vol. 18, no. 11, pp. 53–59, 2011.

[53]   R. K. Blandford, D. K. Morton, S. D. Snow, and T. E. Rahl, "Tensile Stress-Strain Results for 304L and 316L Stainless Steel Plate at Temperature," *Vol. 6 Mater. Fabr.*, pp. 617–628, 2007.

[54]   N. Ramakrishnan and V. S. Arunachalam, "Effective Elastic Moduli of Porous Ceramic Materials," *J. Am. Ceram. Soc.*, vol. 76, no. 11, pp. 2745–2752, 1993.

[55]   a P. Roberts and E. J. Garboczi, "Elastic properties of model porous ceramics," *J. Am. Ceram. Soc.*, vol. 83, no. 12, pp. 3041–3048, 2000.

[56]   W. E. King, H. D. Barth, V. M. Castillo, G. F. Gallegos, J. W. Gibbs, D. E. Hahn, C. Kamath, and A. M. Rubenchik, "Observation of keyhole-mode laser melting in laser powder-bed fusion additive manufacturing," *J. Mater. Process. Technol.*, vol. 214, no. 12, pp. 2915–2925, 2014.

[57]   H. Gong, D. Christiansen, J. Beuth, and J. J. Lewandowski, "Melt Pool Characterization for Selective Laser Melting of Ti-6Al-4V Pre-alloyed Powder," in *Solid Freeform Fabrication Symposium*, 2014, pp. 256–267.

[58]   W. King, A. T. Anderson, R. M. Ferencz, N. E. Hodge, C. Kamath, and S. A. Khairallah, "Overview of modelling and simulation of metal powder bed fusion process at Lawrence Livermore National Laboratory," *Mater. Sci. Technol.*, vol. 31, no. 8, pp. 957–968, 2015.

[59]   W. E. King, A. T. Anderson, R. M. Ferencz, N. E. Hodge, C. Kamath, S. A. Khairallah, and A. M. Rubenchik, "Laser powder bed fusion additive manufacturing of metals; physics, computational, and materials challenges," *Appl. Phys. Rev.*, vol. 2, no. 4, p. 41304, 2015.

[60]   S. A. Khairallah, A. T. Anderson, A. Rubenchik, and W. E. King, "Laser powder-bed fusion additive manufacturing: Physics of complex melt flow and formation mechanisms of pores, spatter, and denudation zones," *Acta Mater.*, vol. 108, pp. 36–45, 2016.

[61]   H. W. Mindt, M. Megahed, N. P. Lavery, M. A. Holmes, and S. G. R. Brown, "Powder Bed Layer Characteristics: The Overseen First-Order Process Input," *Metall. Mater. Trans. A*, pp. 1–12, 2016.

[62]   H. M. Ledbetter, "Stainless-steel elastic constants at low temperatures," *J. Appl. Phys.*, vol. 52, no. 3, pp. 1587–1589, 1981.

[63]   H. M. Ledbetter, N. V. Frederick, and M. W. Austin, "Elastic-constant variability in stainless-steel 304," *J. Appl. Phys.*, vol. 51, no. 1, pp. 305–309, 1980.

[64]   D. Gerlich and S. Hart, "Pressure dependence of the elastic moduli of three austenitic stainless steels," *J. Appl. Phys.*, vol. 55, no. 4, pp. 880–884, 1984.

[65]   H. M. Ledbetter, W. F. Weston, and E. R. Naimon, "Low-temperature elastic properties of four austenitic stainless steels," *J. Appl. Phys.*, vol. 46, no. 9, pp. 3855–3860, 1975.

[66]   P. Shankar, P. Palanichamy, T. Jayakumar, B. Raj, and S. Ranganathan, "Nitrogen redistribution, microstructure, and elastic constant evaluation using ultrasonics in aged 316LN stainless steels," *Metall. Mater. Trans. A*, vol. 32, no. December, pp. 2959–2968, 2001.

[67]   M. Fischer, D. Joguet, G. Robin, L. Peltier, and P. Laheurte, "In situ elaboration of a binary Ti-26Nb alloy by selective laser melting of elemental titanium and niobium mixed powders," *Mater. Sci. Eng. C*, vol. 62, pp. 852–859, 2016.

[68]   J. A. Slotwinski, E. J. Garboczi, and K. M. Hebenstreit, "Porosity Measurements and Analysis for Metal Additive Manufacturing Process Control," vol. 119, pp. 494–528, 2014.

[69]   I. Tolosa, F. Garciandía, F. Zubiri, F. Zapirain, and A. Esnaola, "Study of mechanical properties of AISI 316 stainless steel processed by 'selective laser melting', following different manufacturing strategies," *Int. J. Adv. Manuf. Technol.*, vol. 51, no. 5–8, pp. 639–647, 2010.

[70]   V. Barabash, A. Peacock, S. Fabritsiev, G. Kalinin, S. Zinkle, A. Rowcliffe, J. W. Rensman, A. A. Tavassoli, P. Marmy, P. J. Karditsas, F. Gillemot, and M. Akiba, "Materials challenges for ITER - Current status and future activities," *J. Nucl. Mater.*, vol. 367–370 A, no. SPEC. ISS., pp. 21–32, 2007.

[71]   J. T. Busby, P. J. Maziasz, A. F. Rowcliffe, M. Santella, and M. Sokolov, "Development of high performance cast stainless steels for ITER shield module applications," *J. Nucl. Mater.*, vol. 417, no. 1–3, pp. 866–869, 2011.

[72]   G. Kalinin, V. Barabash, A. Cardella, J. Dietz, K. Ioki, R. Matera, R. T. Santoro, and R. Tivey, "Assessment and selection of materials for ITER in-vessel components," *J. Nucl. Mater.*, vol. 283–287, no. PART I, pp. 10–19, 2000.

[73]   a. a F. Tavassoli, "Assessment of austenitic stainless steels," *Fusion Eng. Des.*, vol. 29, pp. 371–390, 1995.

[74] A. S. for Metals, "Metals Handbook," in *Properties and Selection: Stainless Steels, Tool Materials and Special-Purpose Metals*, Vol. 3, 9t., Americal Society for Metals, 1978, pp. 113–114.

[75] E. Heier and J. Wase, "Fatigue crack growth thresholds - The influence of Young's modulus and fracture surface roughness," vol. 20, no. 10, pp. 737–742, 1998.

[76] B. Li and L. G. Rosa, "Prediction models of intrinsic fatigue threshold in metal alloys examined by experimental data," *Int. J. Fatigue*, vol. 82, pp. 616–623, 2016.

[77] R. a. Hardin and C. Beckermann, "Prediction of the fatigue life of cast steel containing shrinkage porosity," *Metall. Mater. Trans. A Phys. Metall. Mater. Sci.*, vol. 40, no. 3, pp. 581–597, 2009.

(a)   (b)
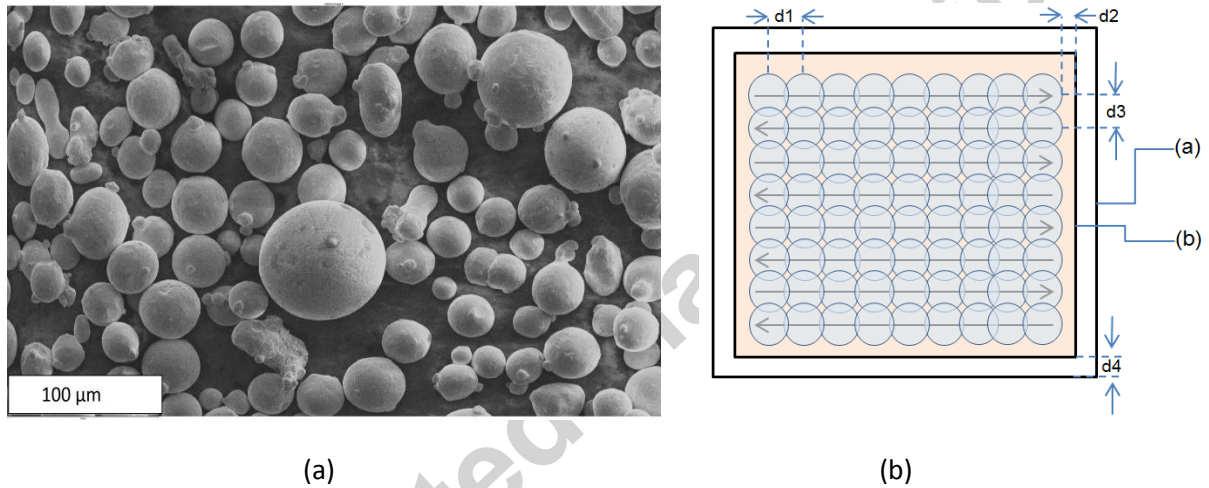
Figure 1 – (a) Virgin 316L powder from Renishaw (b) Meander path pattern, point distance (d1) and hatch space (d3) (Arrow displays direction of laser movement).

(a)   (b)
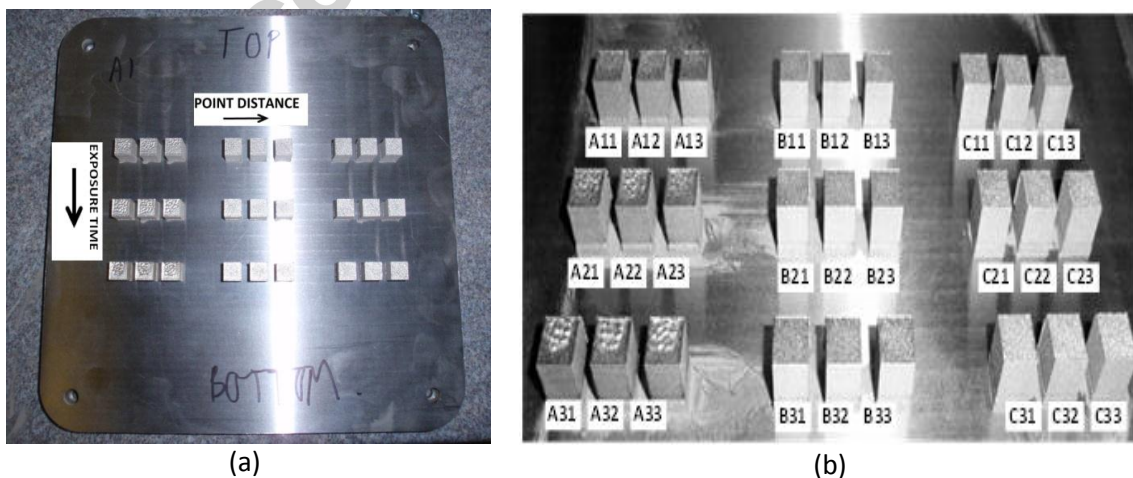
Figure 2 – (a) Layout of machine parameter array on the build plate and (b) as-built sample labels.

24
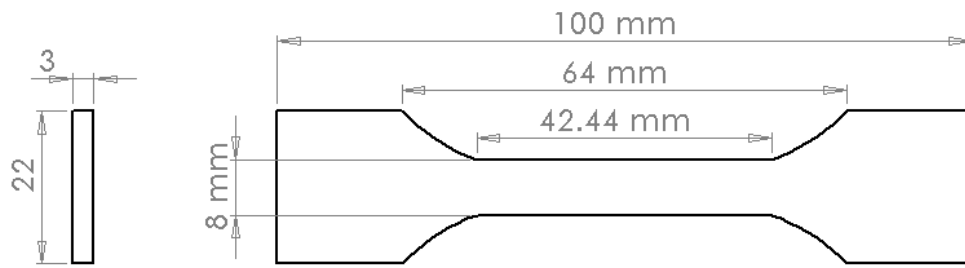
(a) Rectangular cross-section test bar
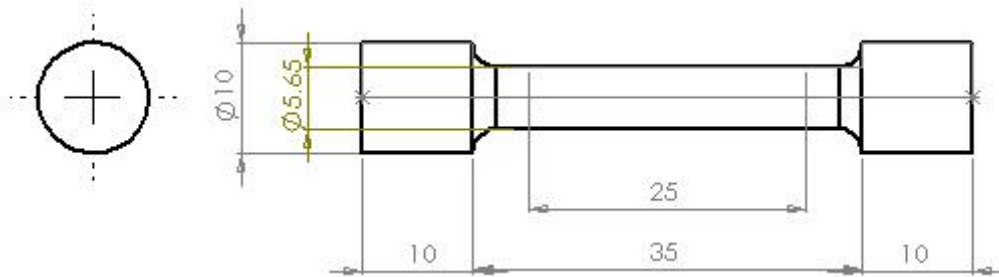
(b) Circular cross-section test bar

Figure 3 –Geometry of test samples used in tensile tests (a) rectangular cross-section (b) circular cross-section.
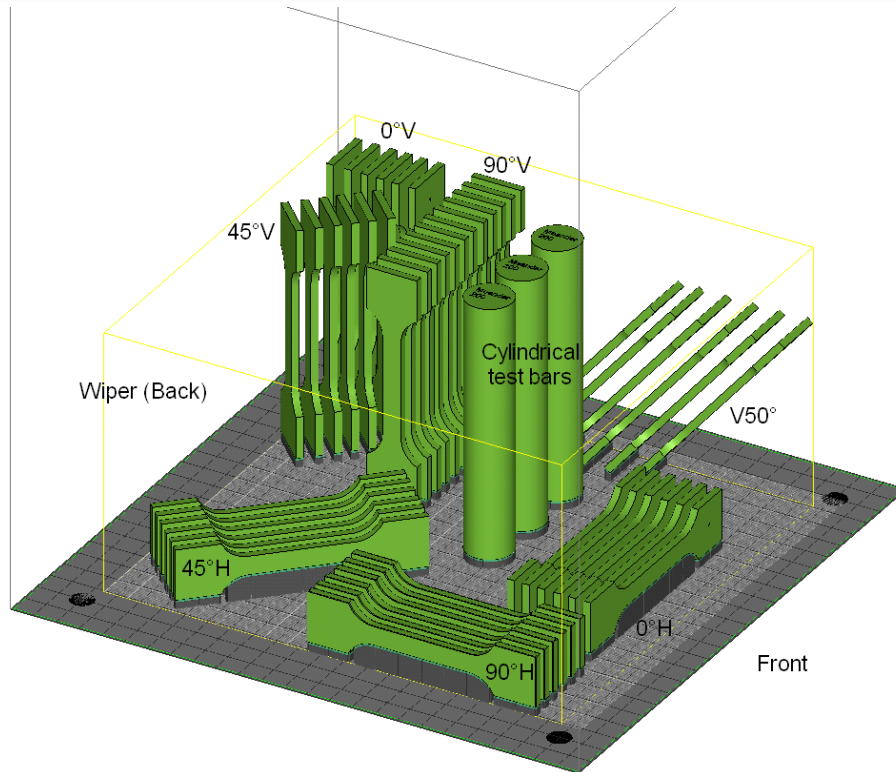
Figure 4 – Layout on the build plate of the rectangular and cylindrical test bars.

(a) C1-3 top SEM 100X

(d) C1-2 top Optical 200X

(b) A3-3 top SEM 100X

(e) A2-3 top Optical 200X

(c) A1-3 top SEM 100X

(f) A1-3 side SEM 100X
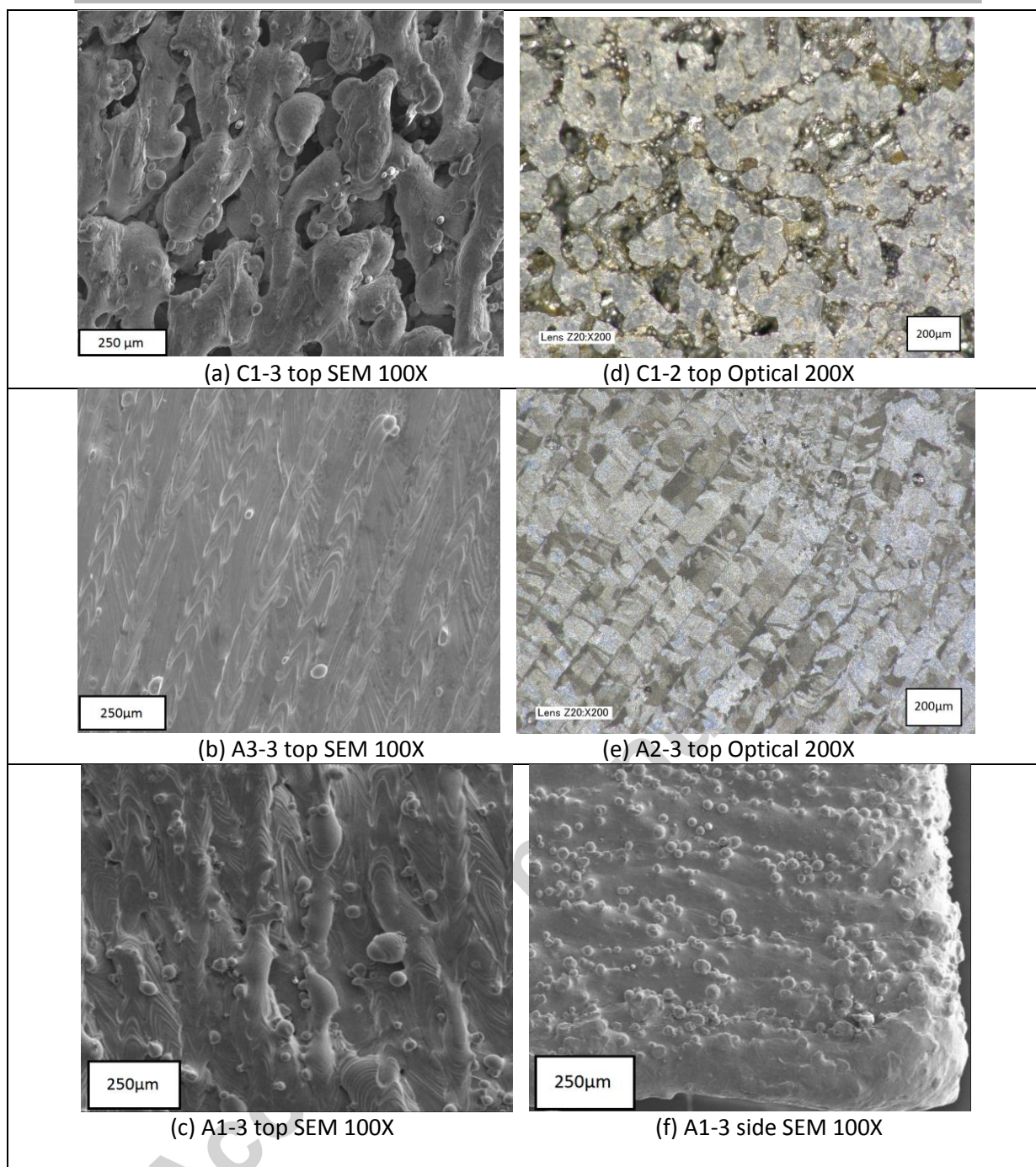
Figure 5 – Low magnification optical and SEM images of the top and sides of the cube samples.
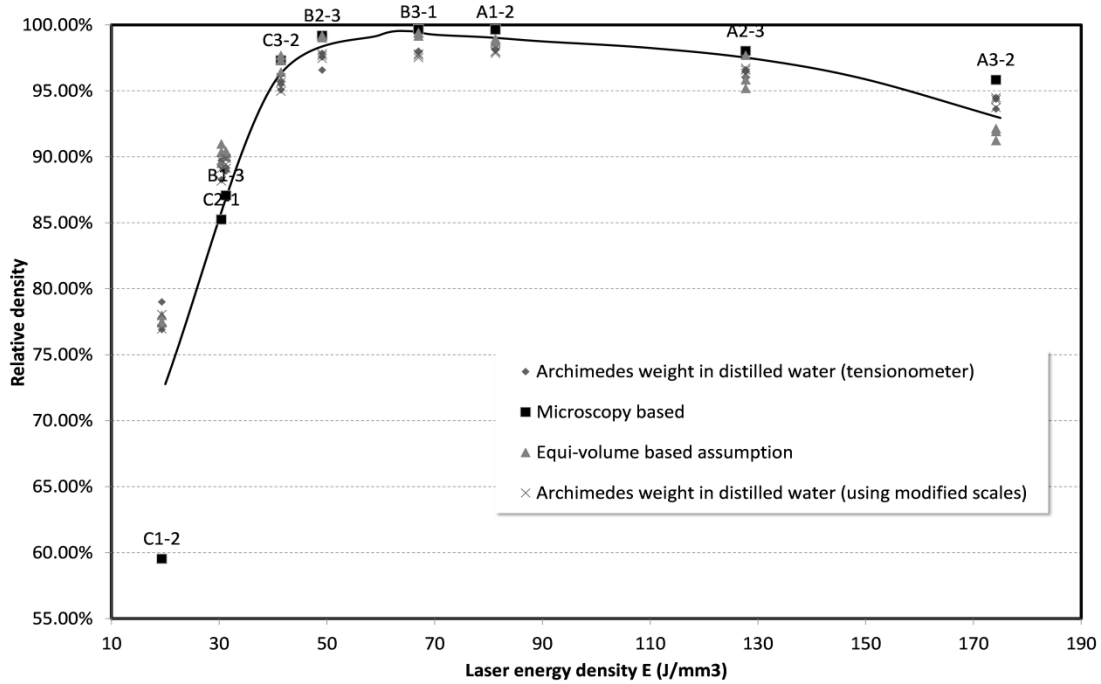
Figure 6 – Relative density with laser input energy, as measured by the different gravimetric based methods for the as-built cubes.
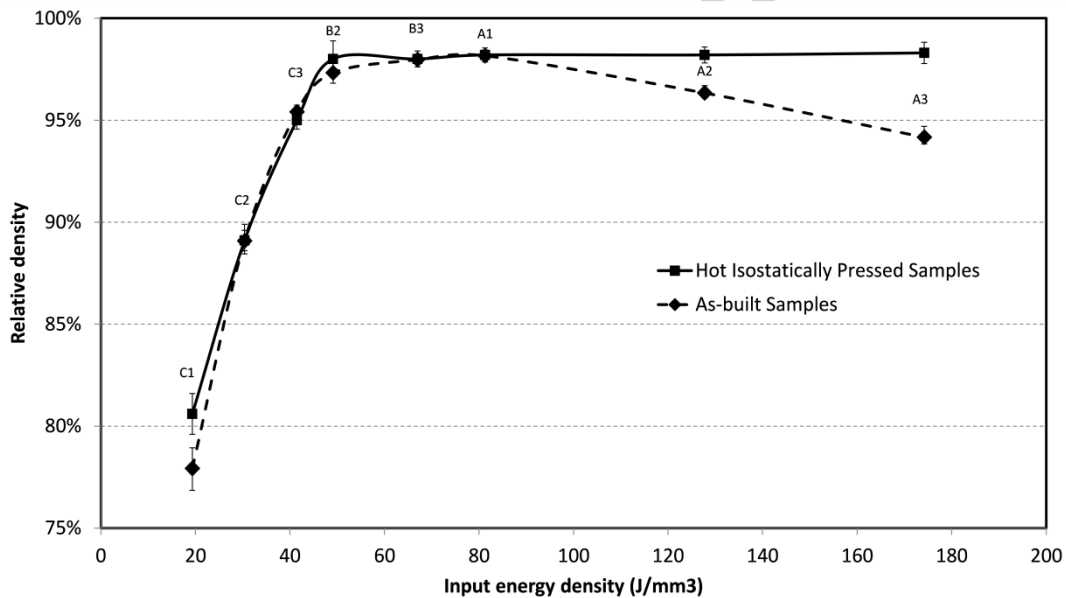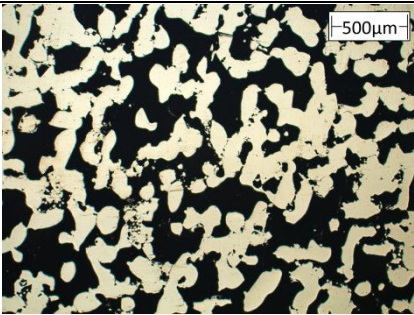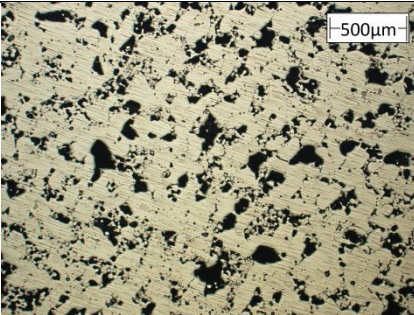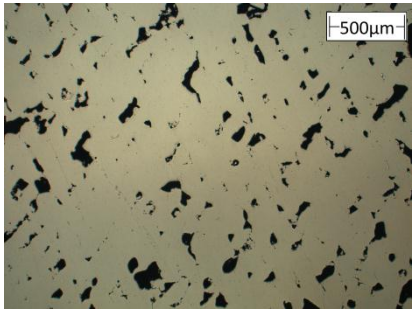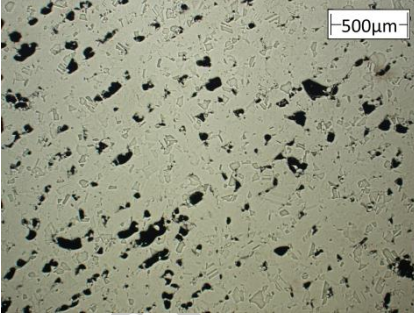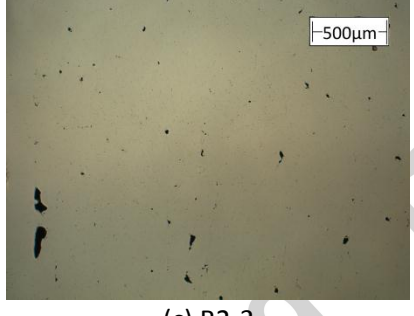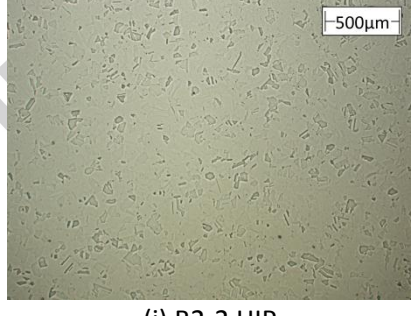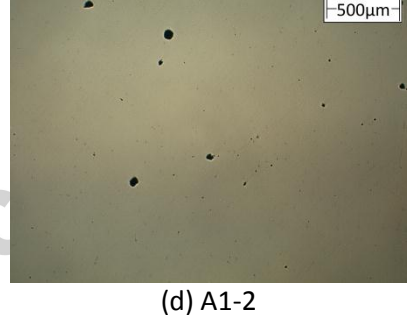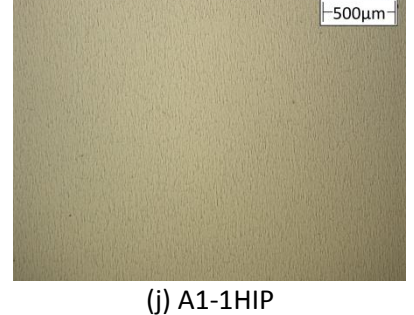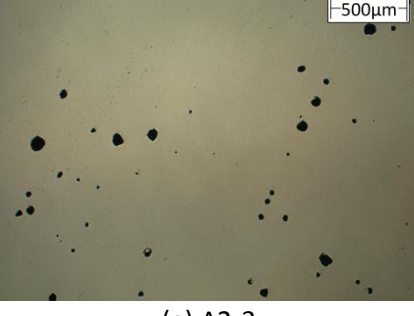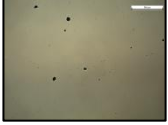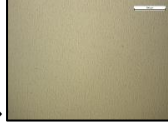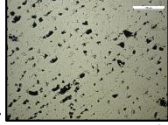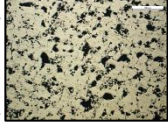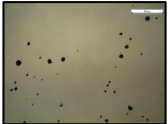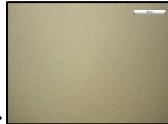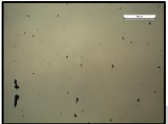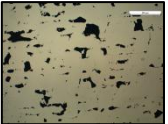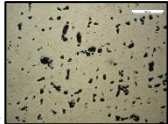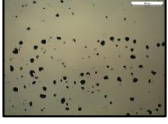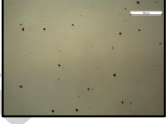
Figure 7 – Comparison of the average relative density (across all gravimetric measurements) of the as-built cubes compared to the hot isostatically pressed cubes.

Laser energy density (J/mm³)	As-built samples	Hot isostatically pressed samples
19.36	(a) C1-2	(g) C1-1HIP
31.27	(b) B1-3	(h) B1-1HIP
49.13	(c) B2-3	(i) B2-2 HIP
81.29	(d) A1-2	(j) A1-1HIP
127.74	(e) A2-3	(k) A2-2HIP

174.19		
	(f) A3-2	(l) A3-1HIP
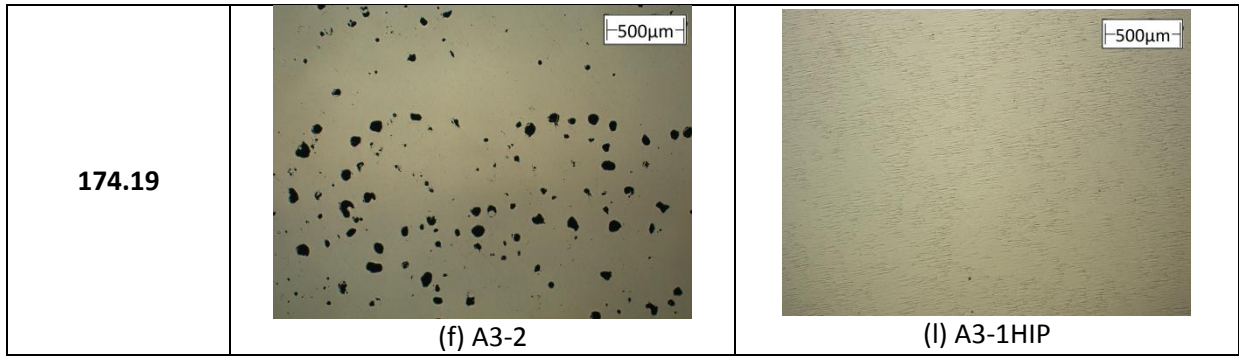
Figure 8 – Microstructure of cube samples before (left) and after hot isostatic pressing (right). Note the higher fraction of porosity, as well as larger, more irregular pores at the lower density.

Figure 9 – Changes in porosity (%) measured using optical image analysis due to hot isostatic pressing for varying point distance (A - 25 μm, B - 65 μm, C - 105 μm) and exposure time (1 - 70 μs, 2 - 110 μs, 3 - 150 μs).
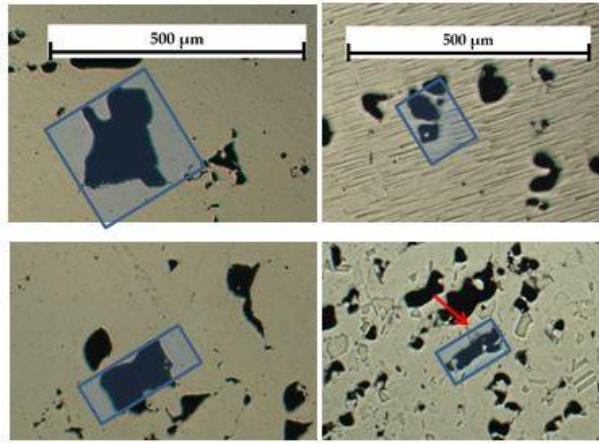
Figure 10 – Suggested pore closing mechanism during hot isostatic pressing resulting in elongated porosity
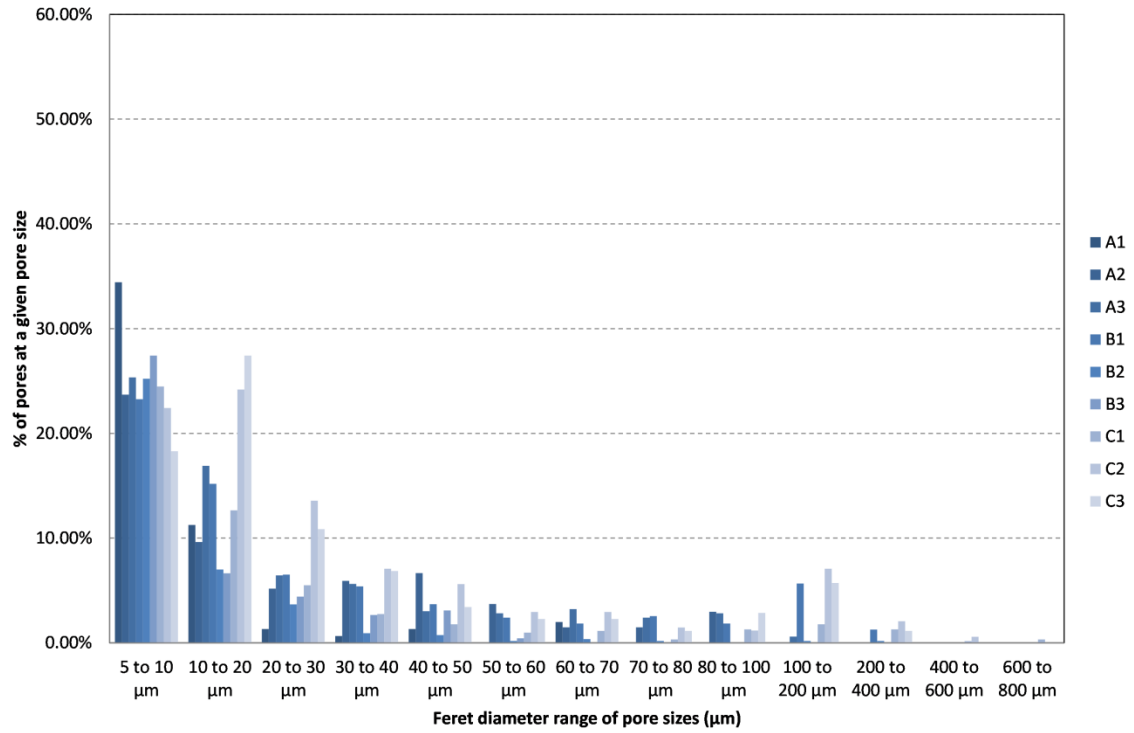
Figure 11 – Distributions of Feret diameters of pore sizes for as-built samples.
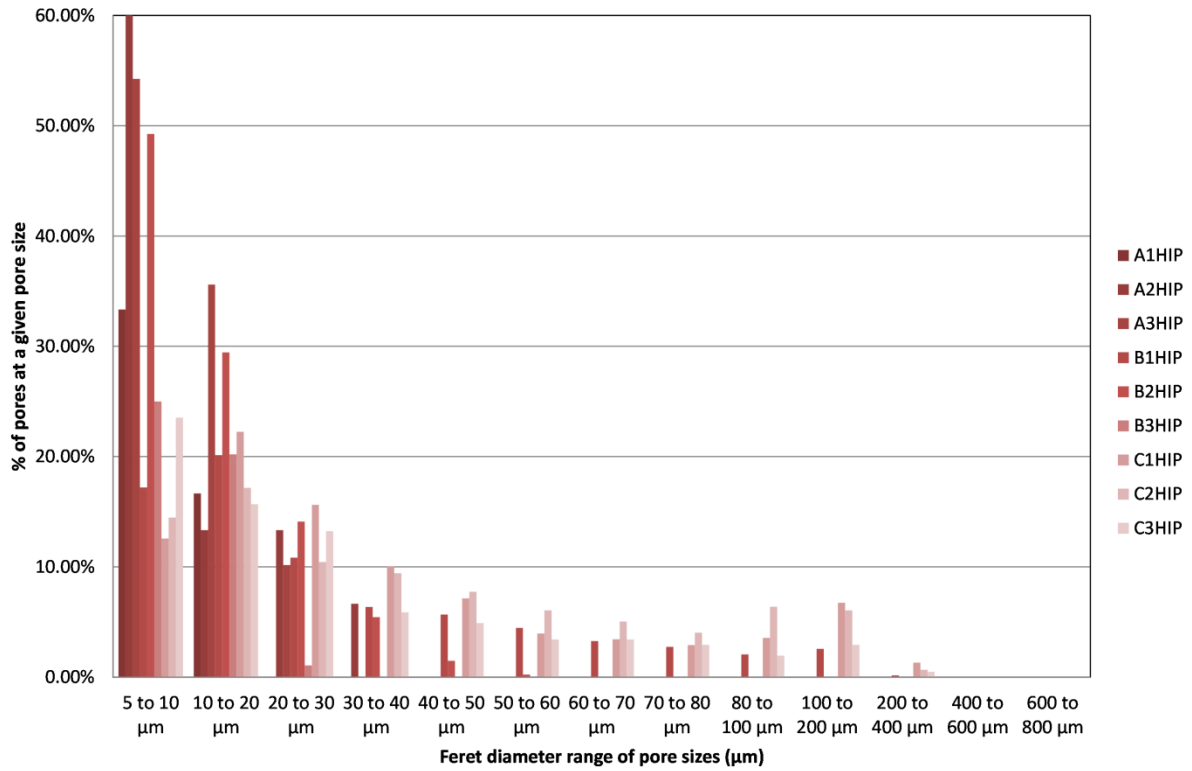
Figure 12 – Distributions of Feret diameters of pore sizes for hot isostatically pressed samples.
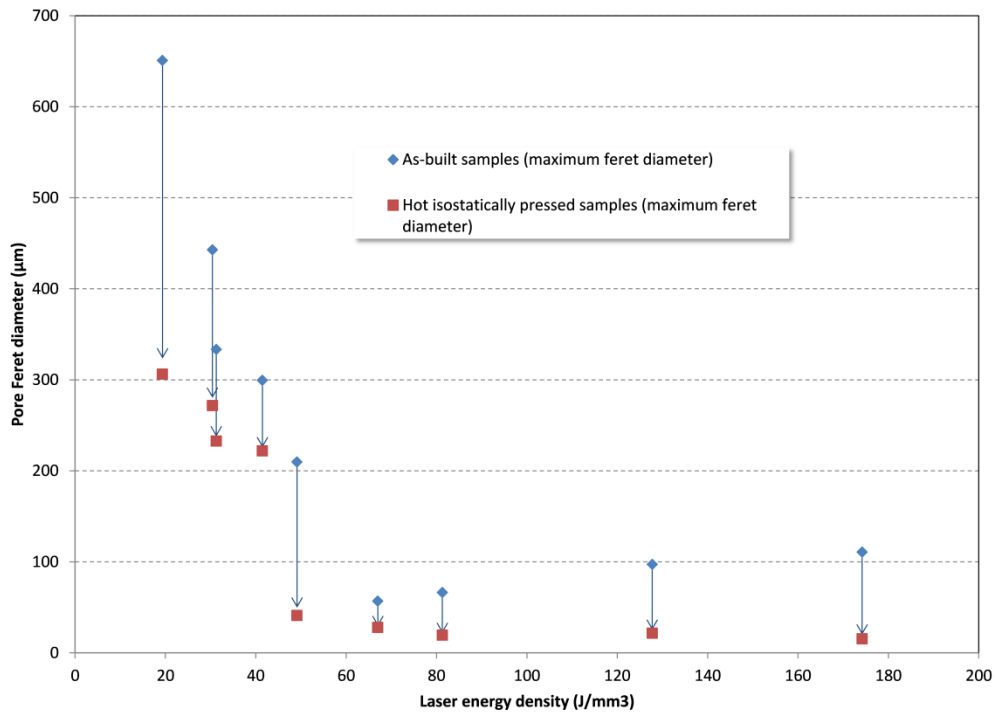
Figure 13 – Maximum Feret diameter of the pores as a function of laser energy density for both as-built and hot isostatically pressed samples.
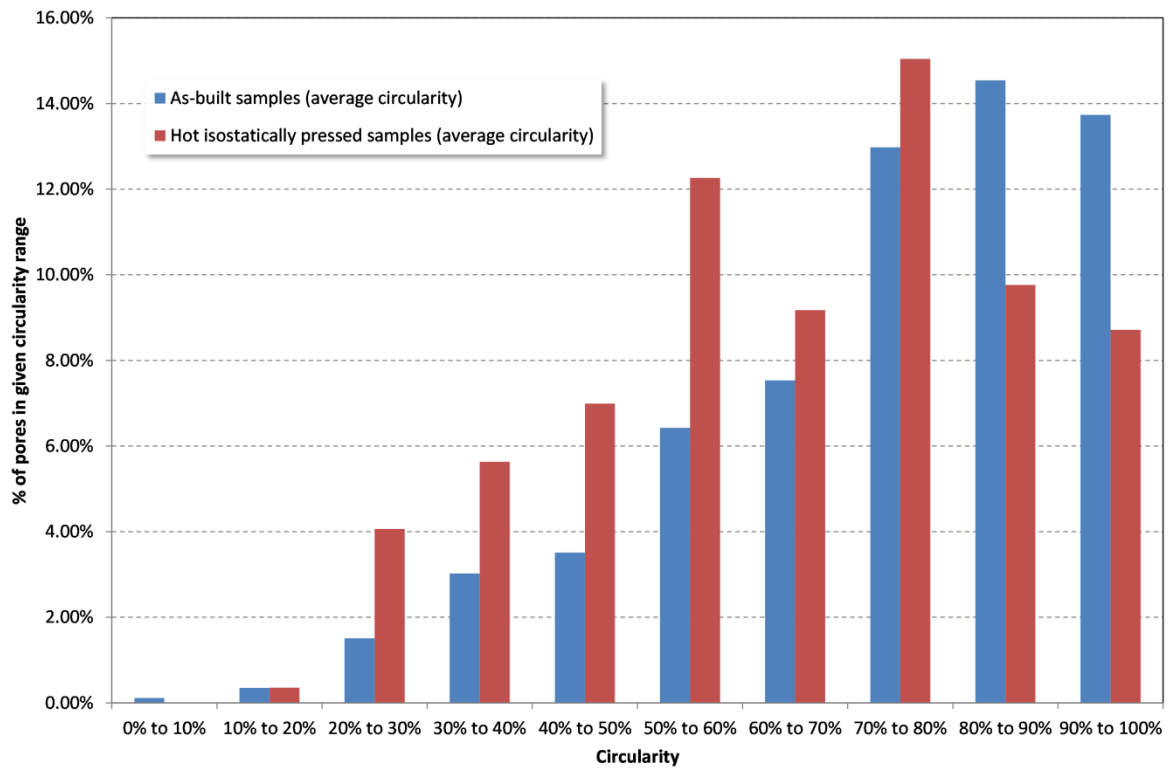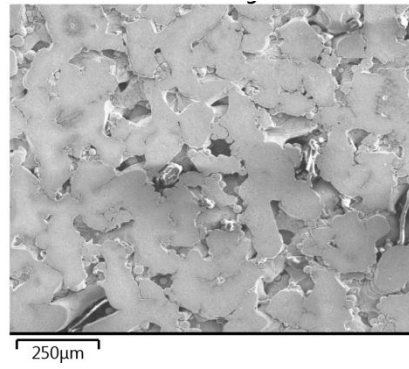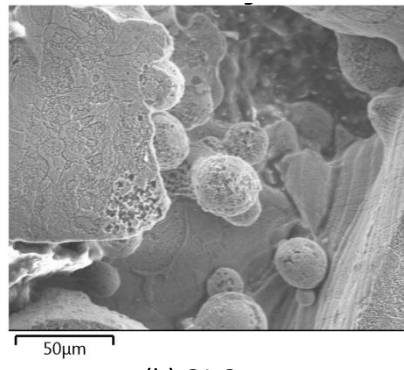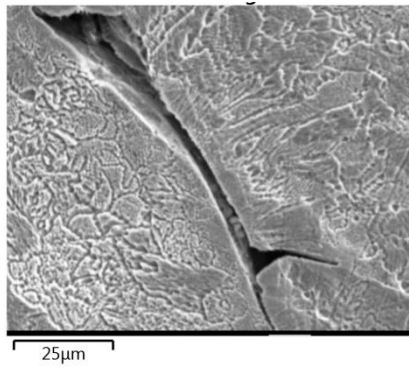
32

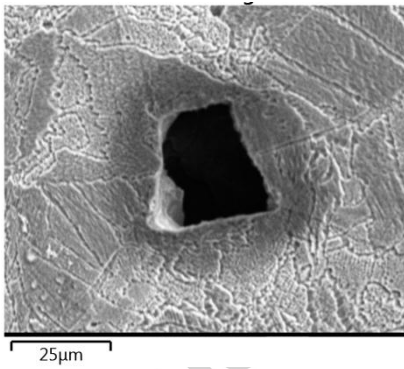**Figure 14 – Distributions of circularity index of pores for as-built compared to hot isostatically pressed samples.**
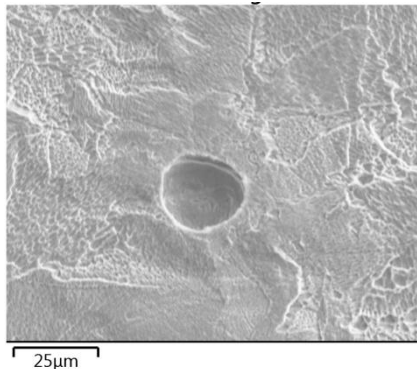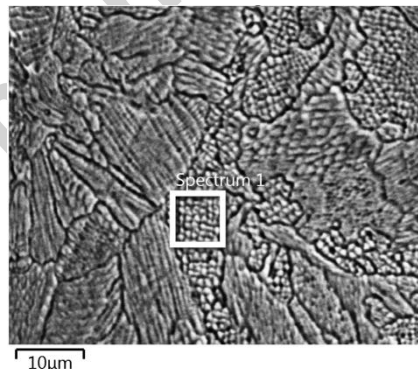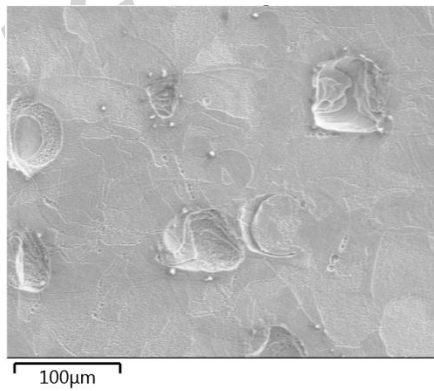
(a) C1-2

(b) C1-2

(c) B2-3

(d) B2-3

(e) A1-2

(f) C1-2 SEM image

(g) A3-2
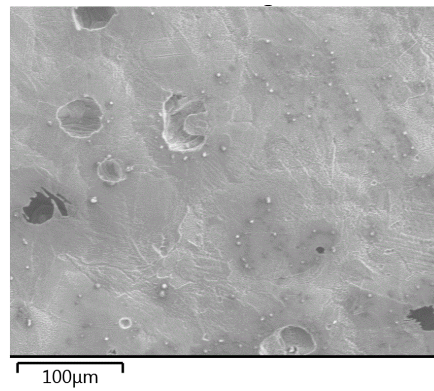
(h) A3-2

Figure 15 – Close-up images showing morphology of as-built porosity taken on the SEM.

(a) B23-as-built (highest mag)

(d) B22-HIPped (highest mag)

(b) B23-as-built (high mag)

(e) B22-HIPped (high mag)

(c) B23-as-built (low mag)
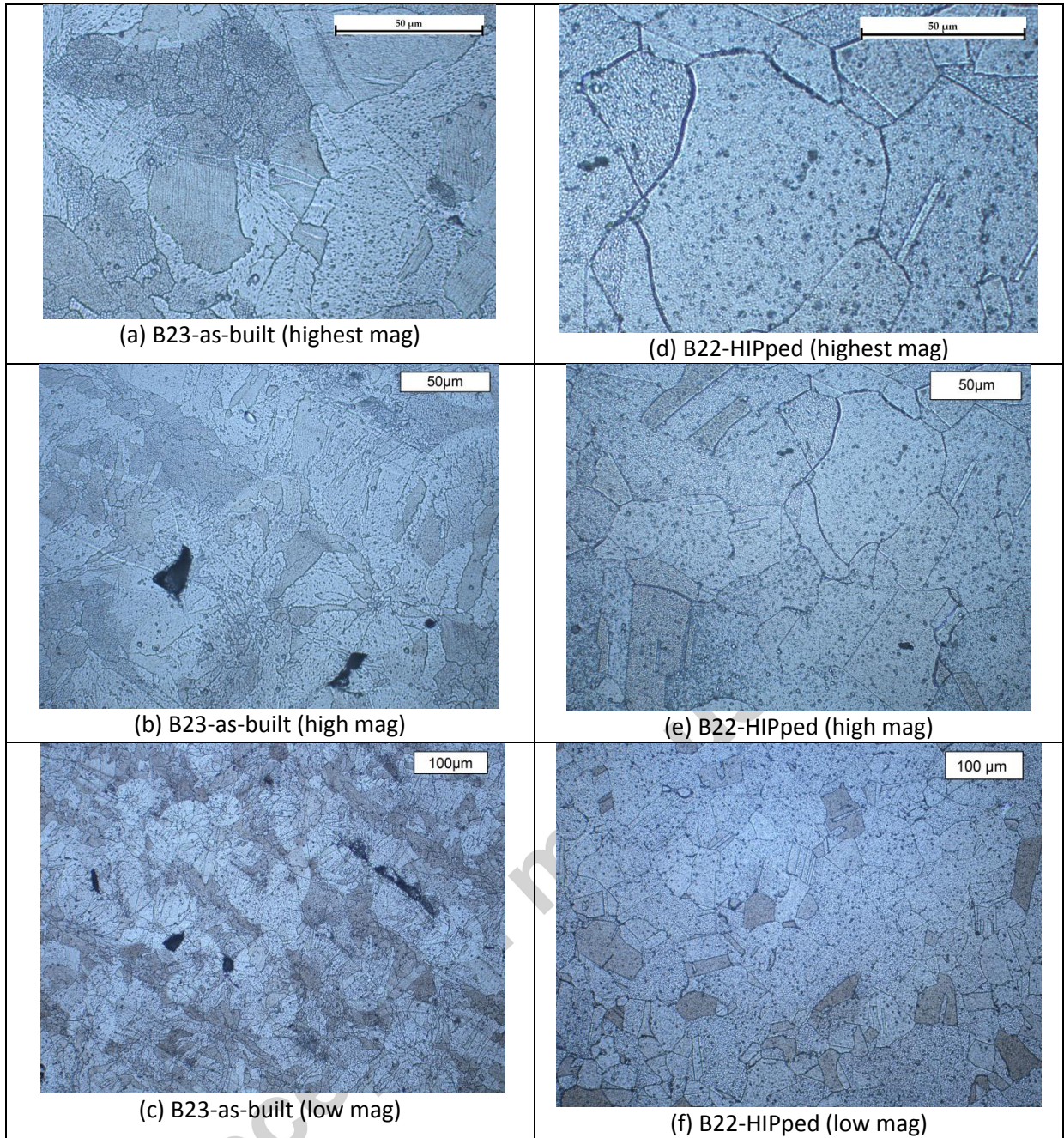
(f) B22-HIPped (low mag)

Figure 16 – Etched microstructure comparing as-built and hot isostatically pressed cubes.

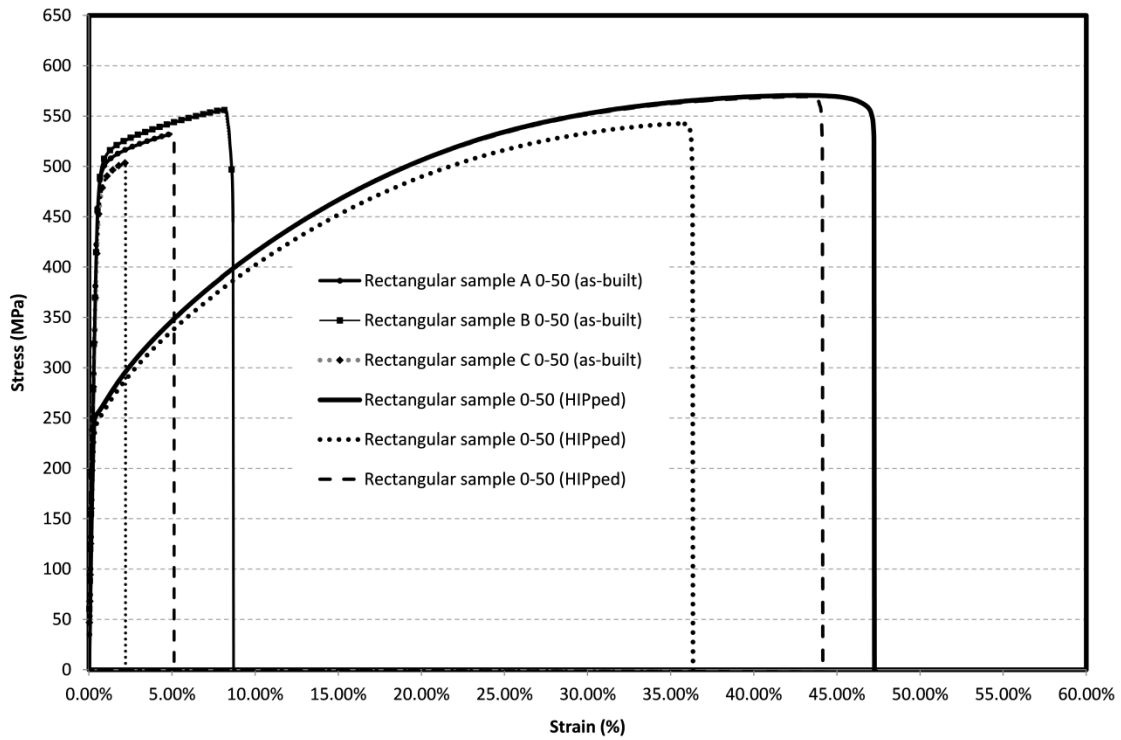**Figure 17 – Tensile test results for bars built at 50° to the vertical and using rectangular cross-section test bar, as-built versus hot isostatically pressed.**
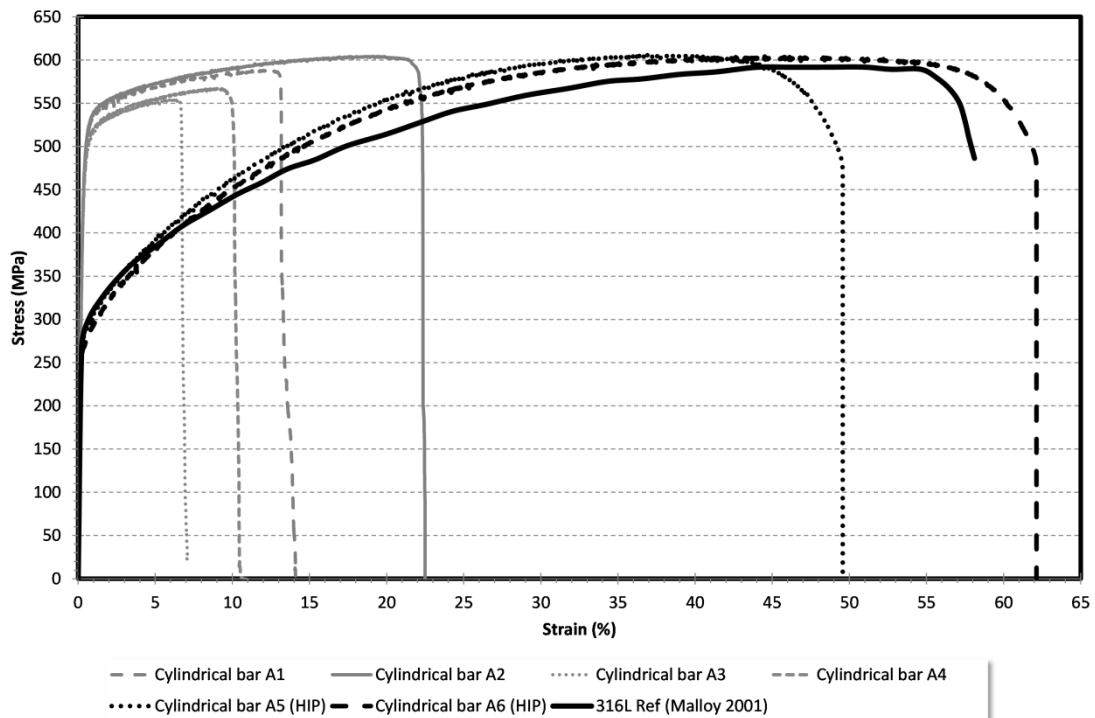

Figure 18 - Tensile tests from cylindrical test bars, as-built versus hot isostatically pressed.

36
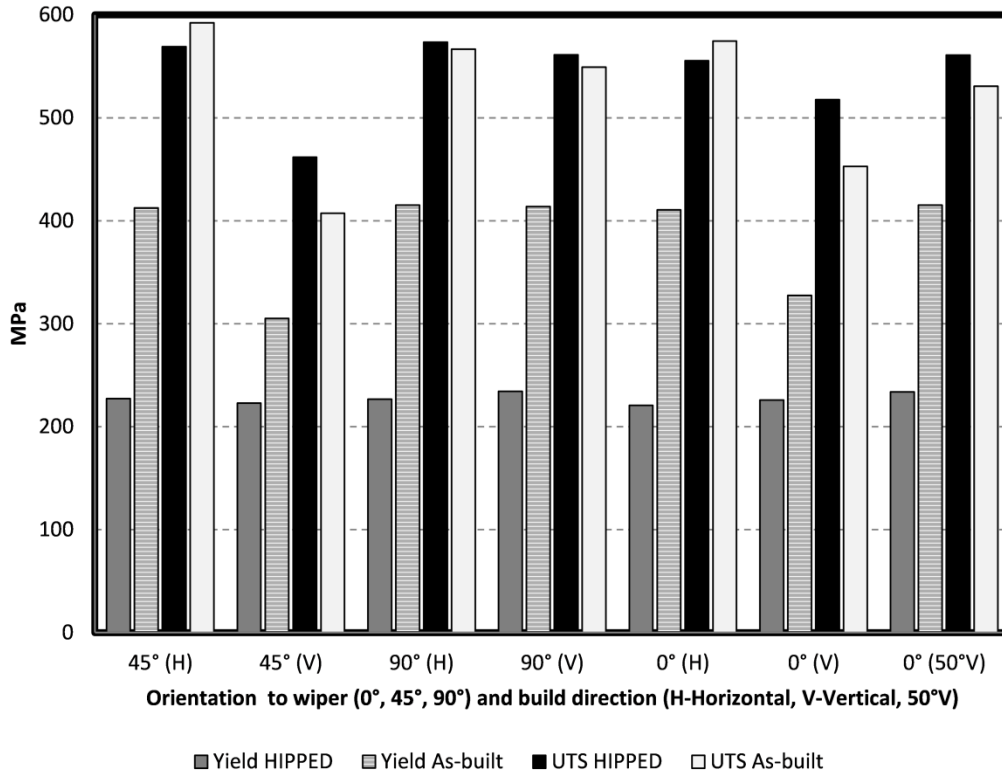
Figure 19 – Averaged Yield Stress and Upper Tensile Stress for rectangular components.
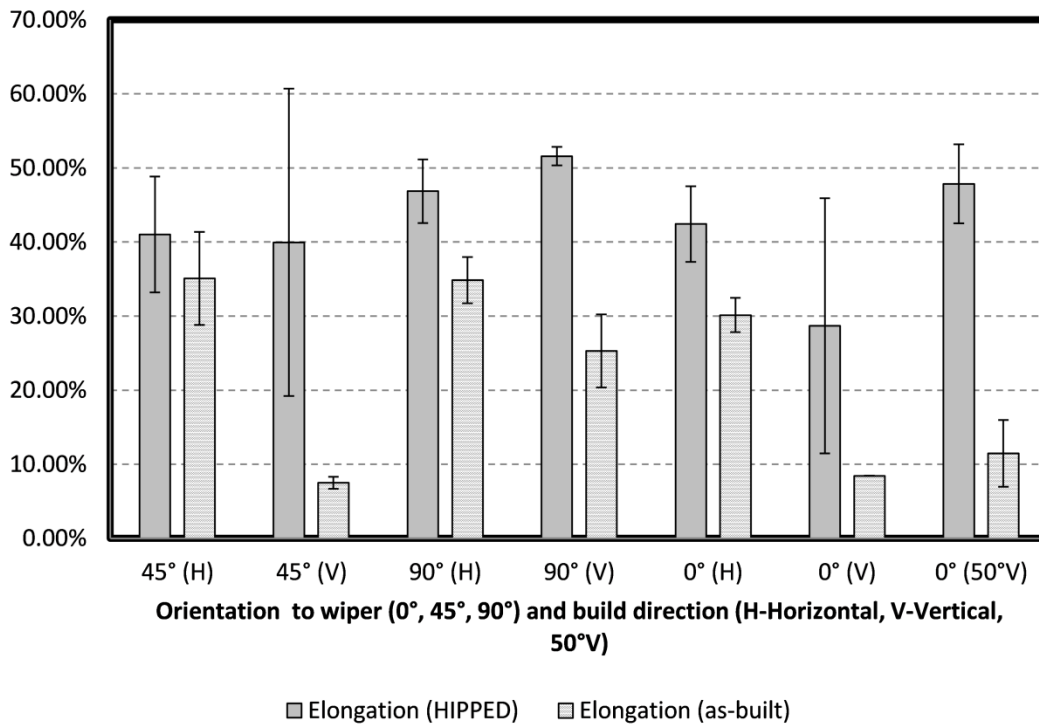
Figure 20 – Averaged elongation for rectangular components.
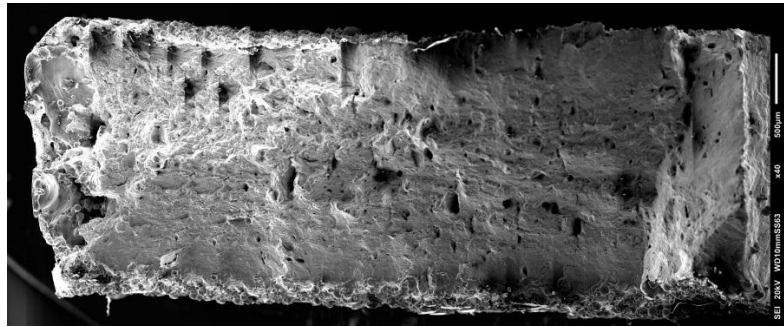
(a) Fracture surface of horizontally built test bar tested in as-built condition
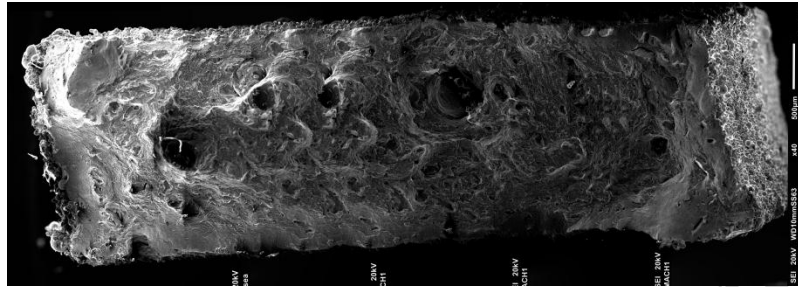
(b) Fracture surface of vertically built test bar tested in as-built condition
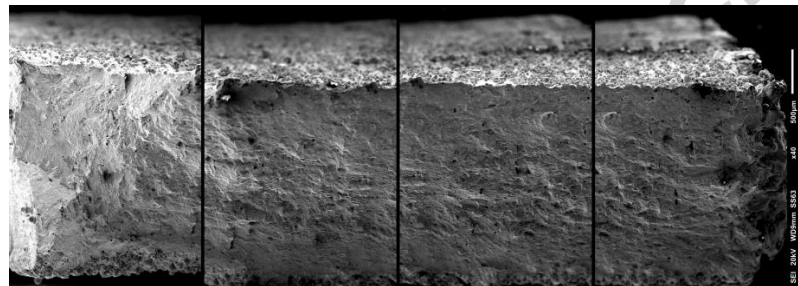
(c) Fracture surface of horizontally built test bar tested after hot isostatic pressing
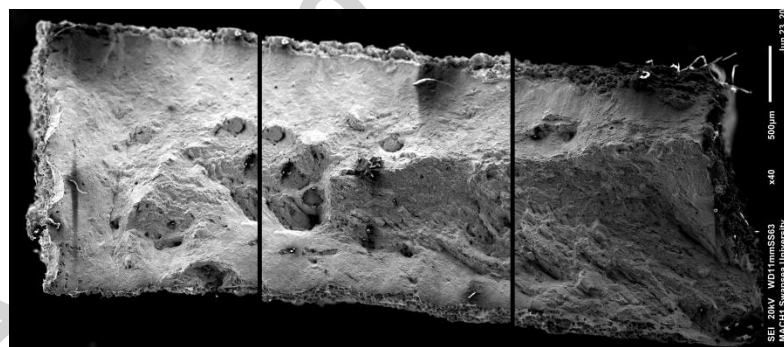
(d)) Fracture surface of vertically built test bar tested after hot isostatic pressing

Figure 21 - Fracture surfaces taken from tensile test, (a) horizontally as-built (v) vertically as-built, (c) horizontally built and hot isostatically pressed and (d) vertically built and hot isostatically pressed.

SEI 20kV WD10mmSS63 x1,900 10µm
MACH1 Swansea University Jun 24, 2016

(a)

SEI 20kV WD10mmSS63 x1,900 10µm
MACH1 Swansea University Jun 24, 2016
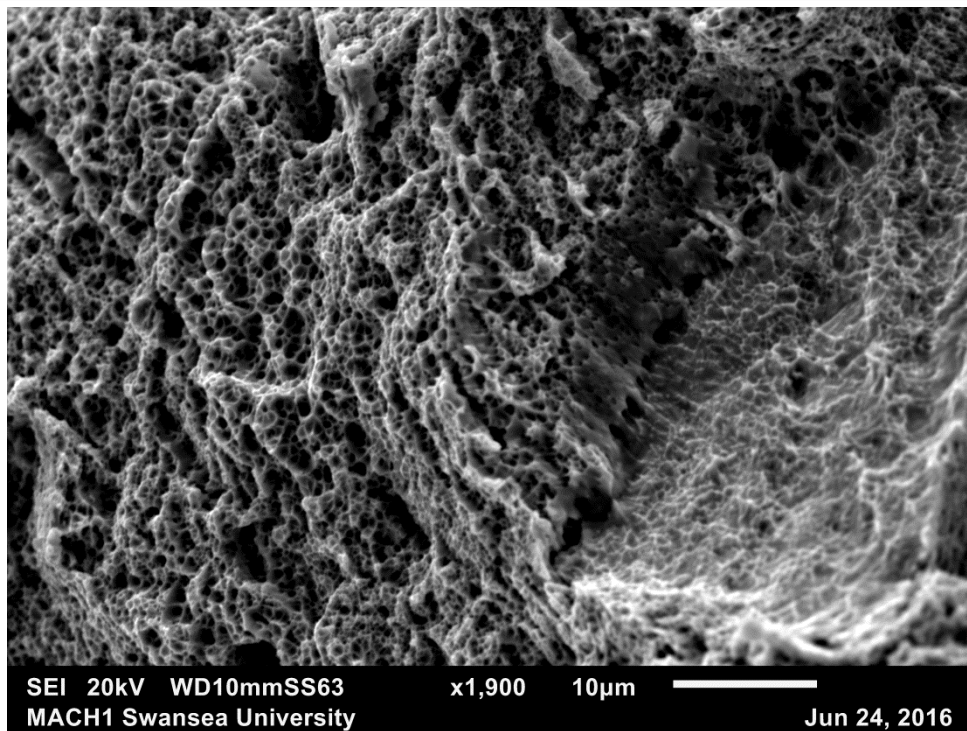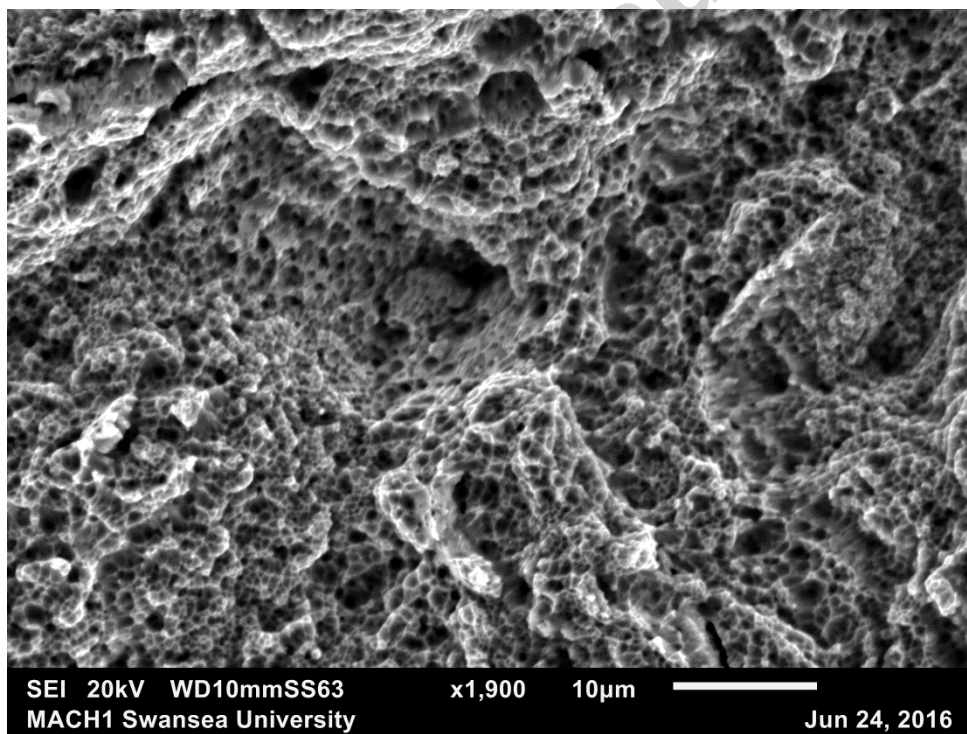
(b)

Figure 22 - Fracture surfaces taken from as-built tensile tests (a) horizontal and (b) vertical.

39

SEI 20kV WD8mm SS63   x1,900   10µm
MACH1 Swansea University   Jun 24, 2016

(a)

SEI 20kV WD10mmSS63   x1,900   10µm
MACH1 Swansea University   Jun 24, 2016
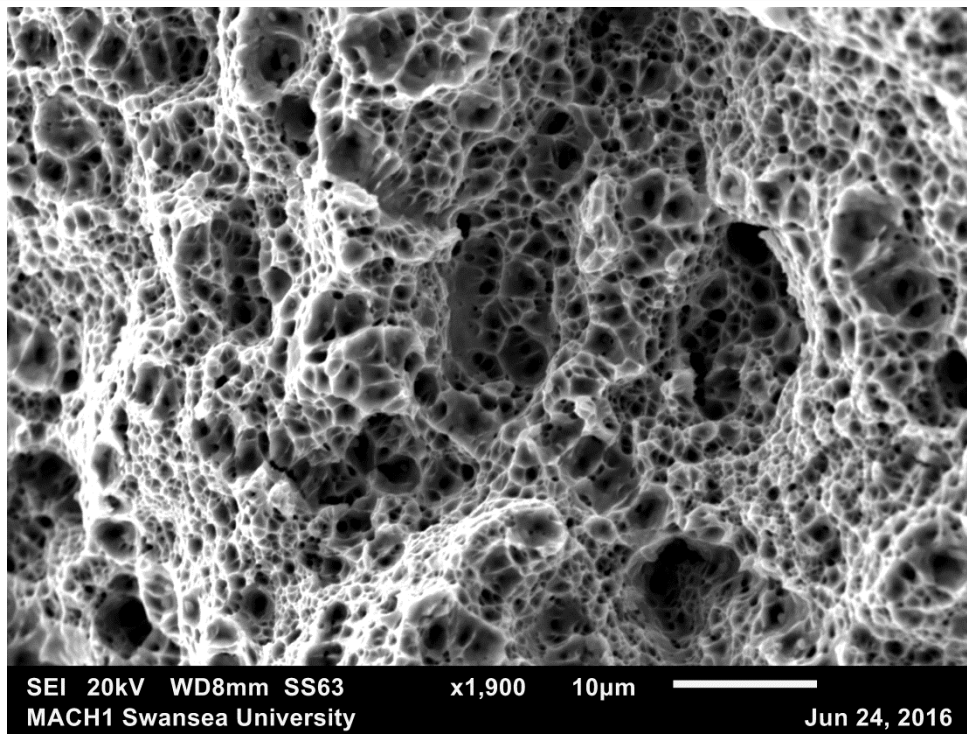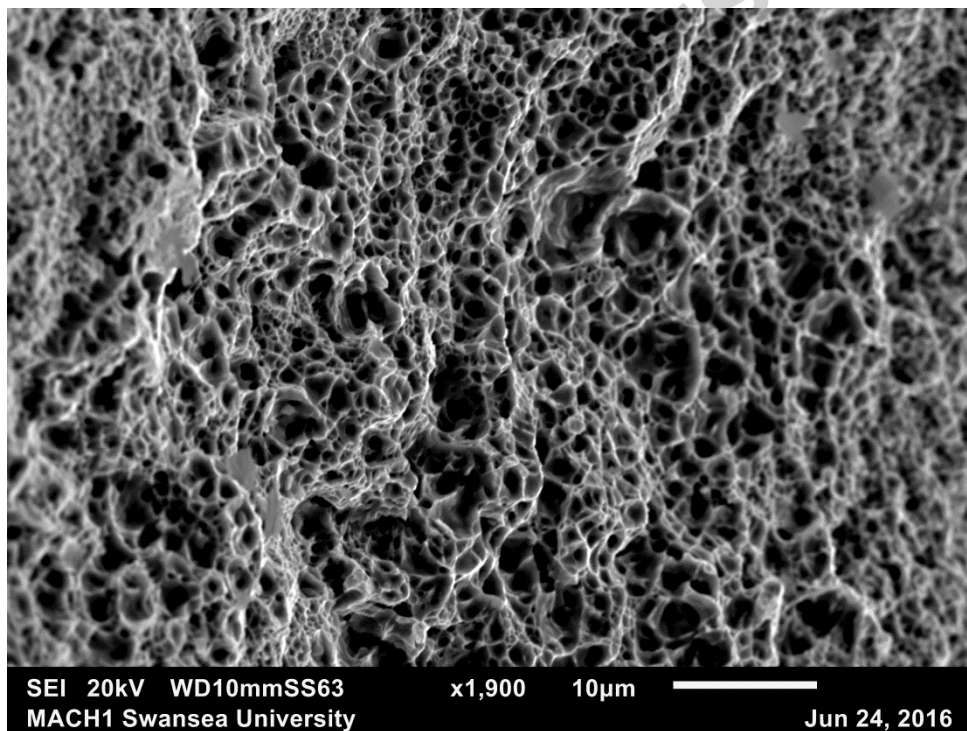
(b)

Figure 23 - Fracture surfaces taken from hot isostatically treated tensile test bars (a) horizontally built and (b) vertically build.

SEI 20kV WD10mmSS63 x3,000 5μm
MACH1 Swansea University Jun 24, 2016

(a)

SEI 20kV WD10mmSS63 x3,000 5μm
MACH1 Swansea University Jun 24, 2016
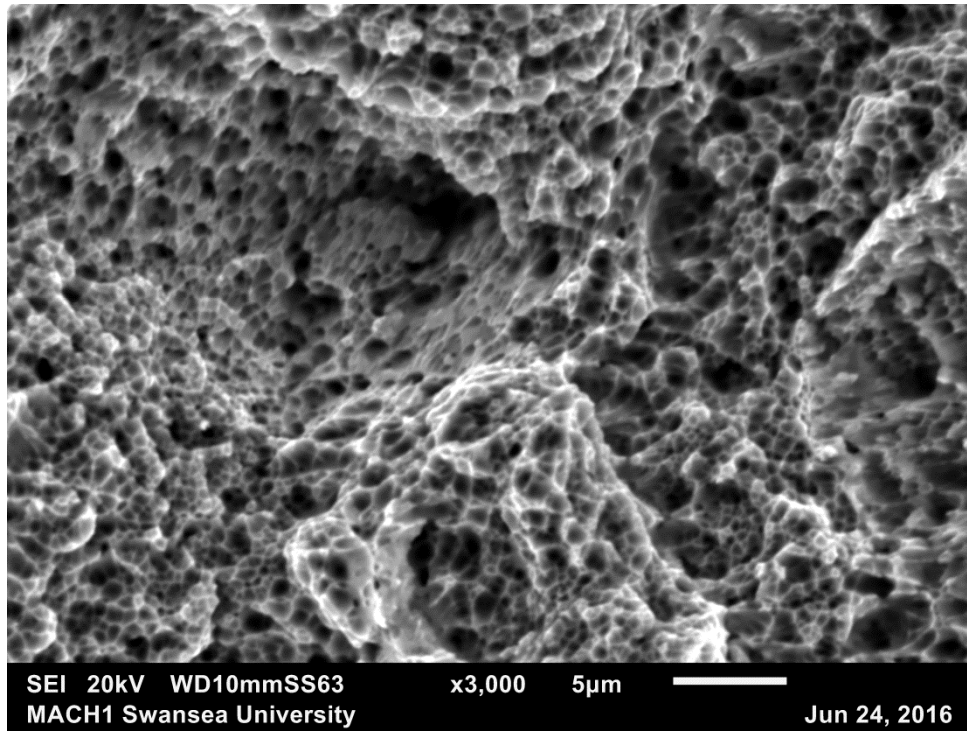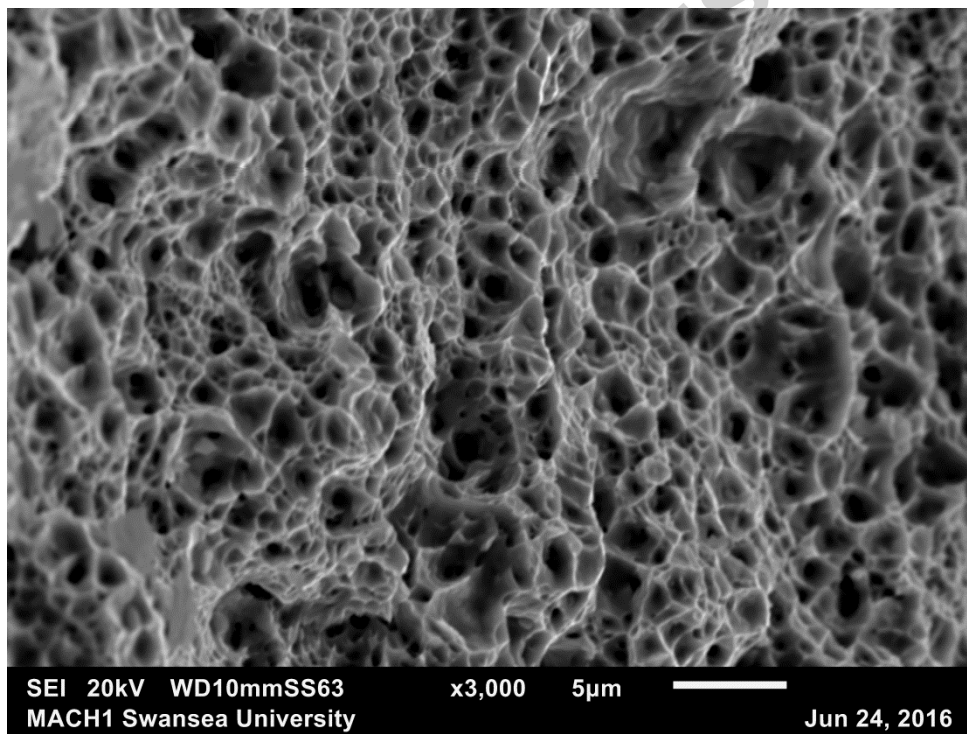
(b)

Figure 24 - Fracture surfaces taken from tensile test bars (a) horizontally as-built (b) horizontally built and hot isostatically pressed (3000X magnification).
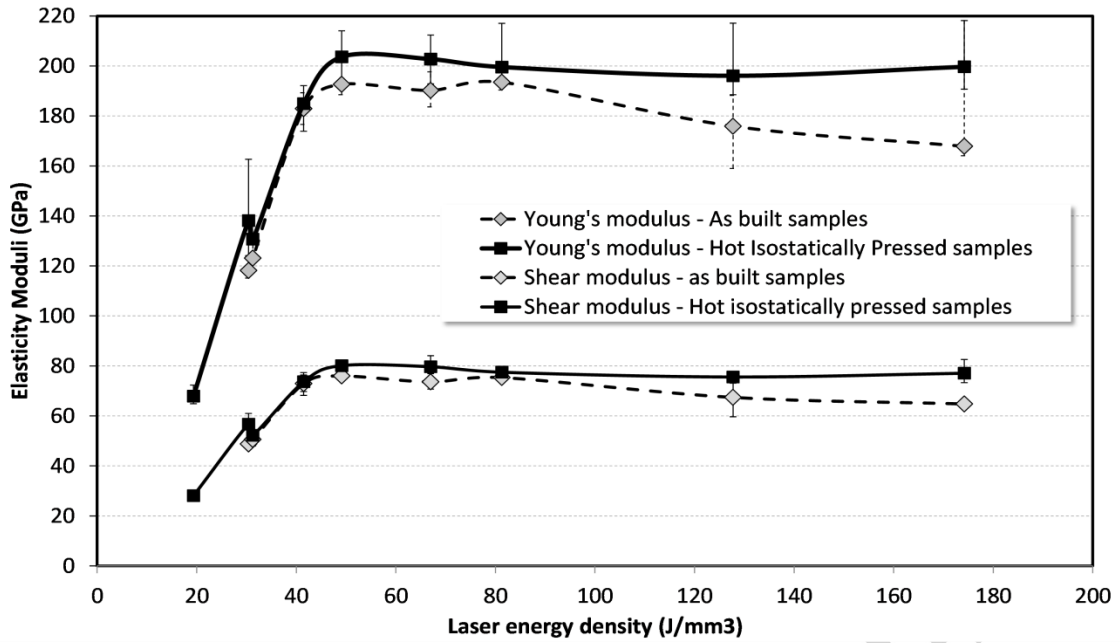
Figure 25 – Young's modulus and shear modulus as calculated using the ultrasound measurements.
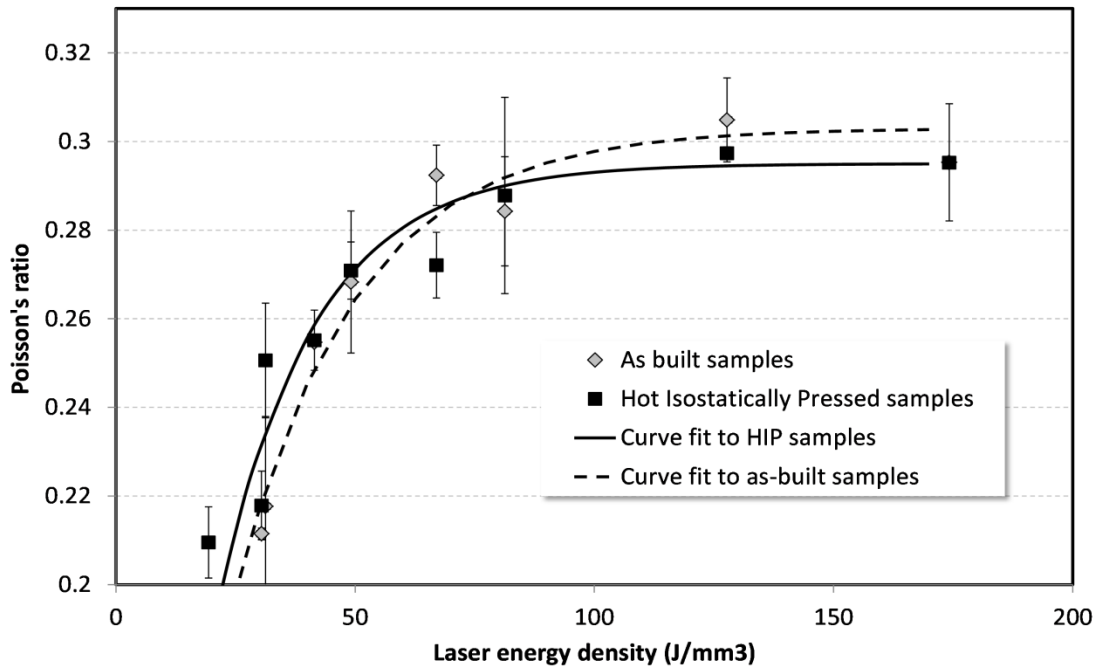
Figure 26 – Poisson's ratio as calculated from ultrasound measurements comparing the as-built and hot isostatically pressed cubes.

42
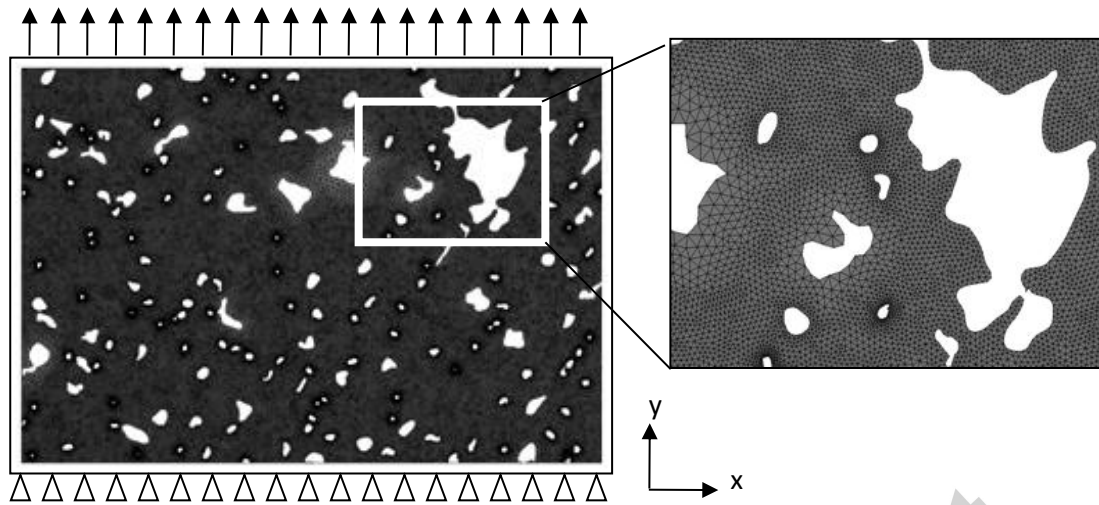
Figure 27 – Typical finite element mesh and boundary condition for the stress analysis of the microstructure.
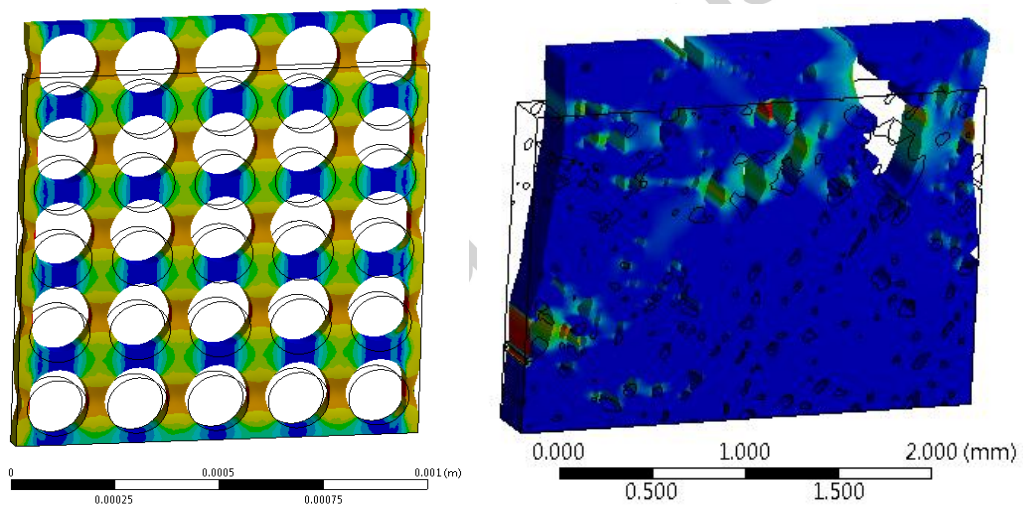
Figure 28 – Typical stress results and a deformed geometry (x10).

Porosity =1.8%			
Porosity =7.1%			
Porosity =44.2%			
Porosity =11.3%			
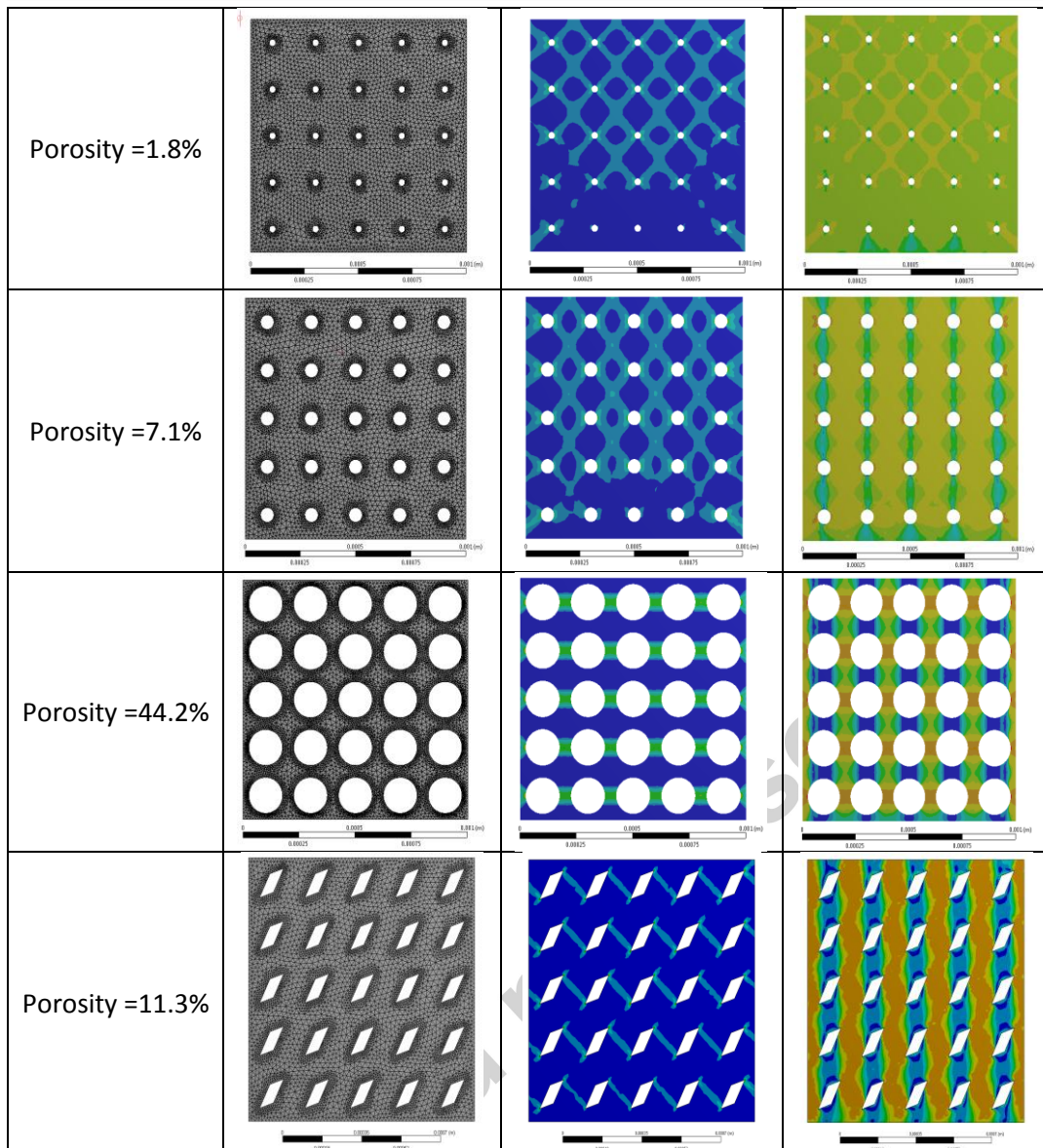
Figure 29 – FEA simulations of geometries with an ordered and increasing porosity.

44

(a) Pore distribution

(b) FE mesh

(c) Von Misses stresses

(d) Equivalent plastic strain

(e) Total deformation

(f) Geometry scaled by deformation
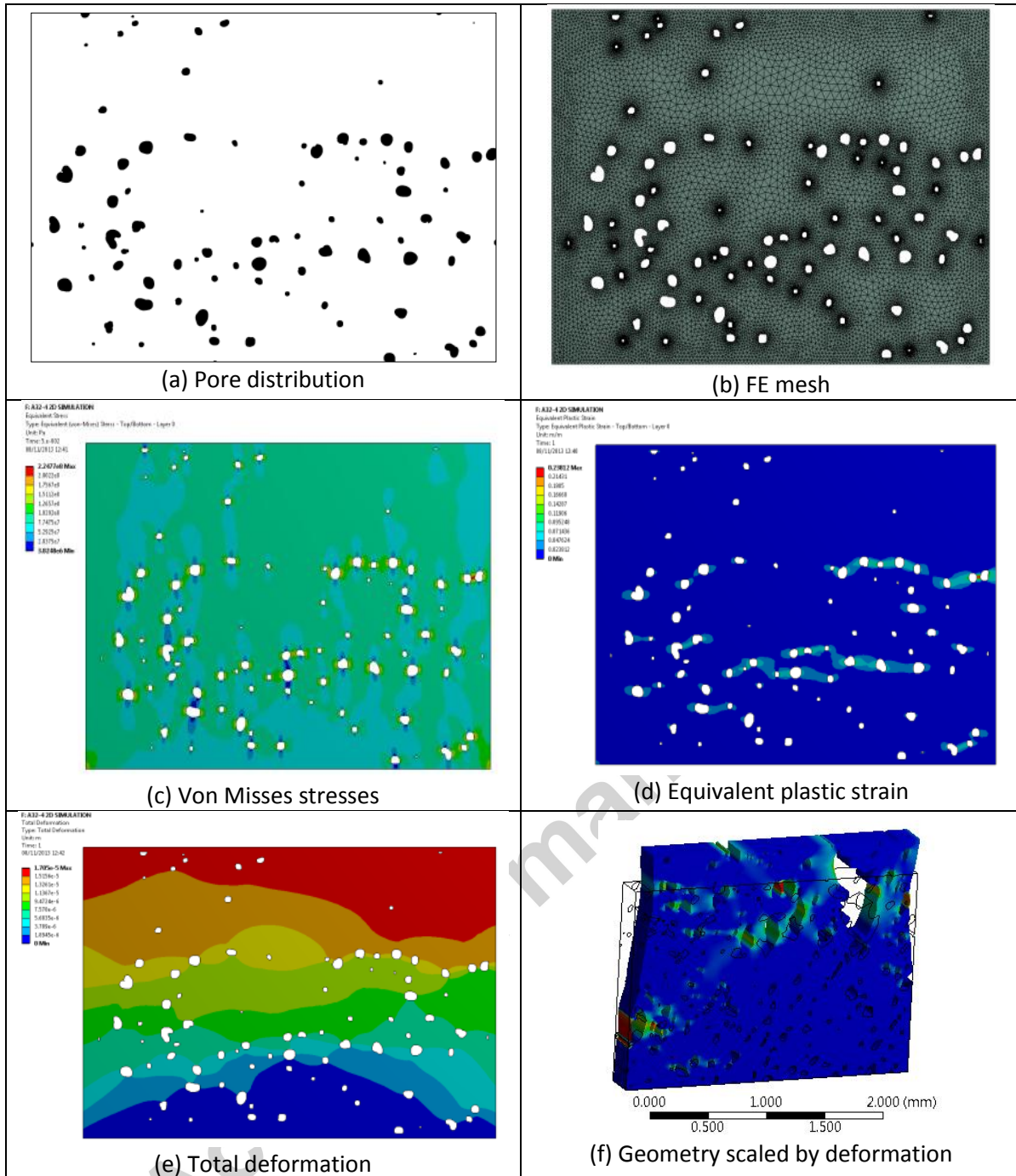
Figure 30 – FE analysis results for porosity derived from the optical microscope images for samples A32 (4.18% porosity).

(a) Pore distribution

(b) FE mesh

(c) Von Misses stresses

(d) Equivalent plastic strain

(e) Total deformation
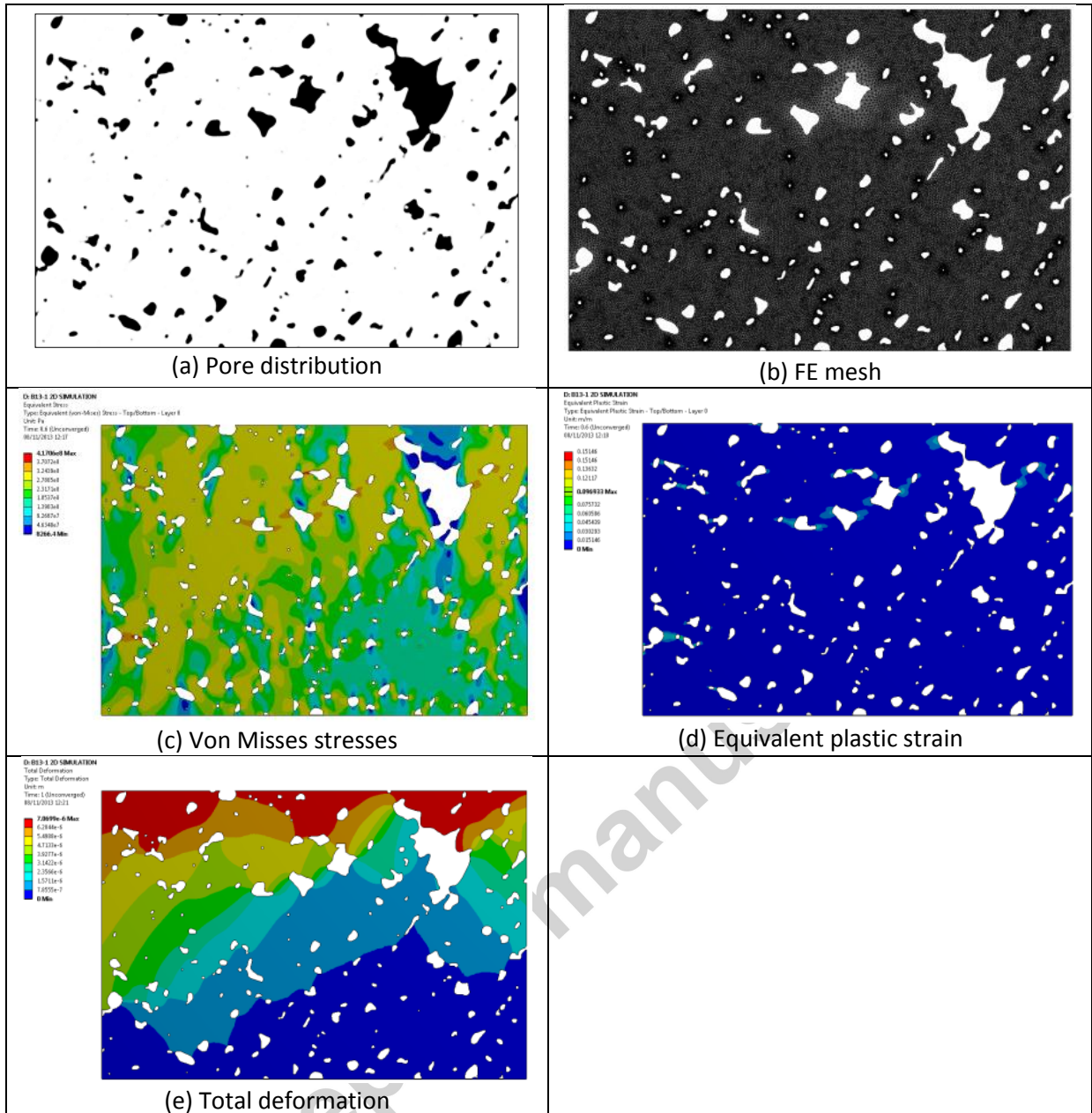
Figure 31 – FEA simulations with porosity derived from the optical microscope images for samples B13 (12.94% porosity).

46
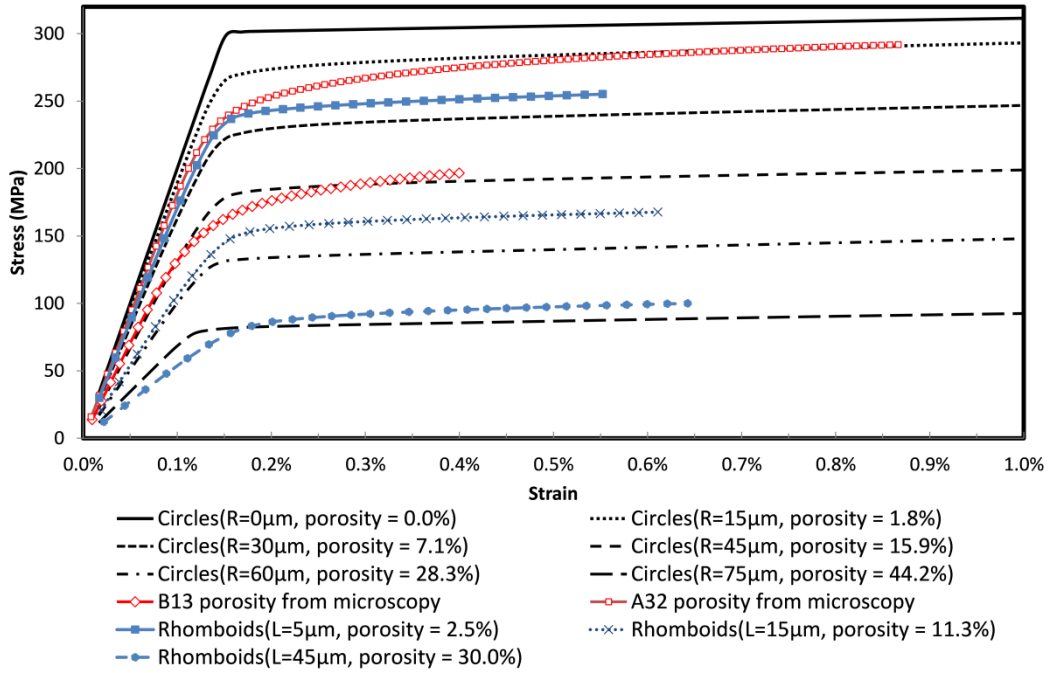
Figure 32 – Finite element based stress-strain curves for ordered circular (0-44% porosity) and rhomboidal porosity (2.5-30% porosity), and porosity derived from A32 (4.18% porosity) and B13 (12.94% porosity) micrographs.
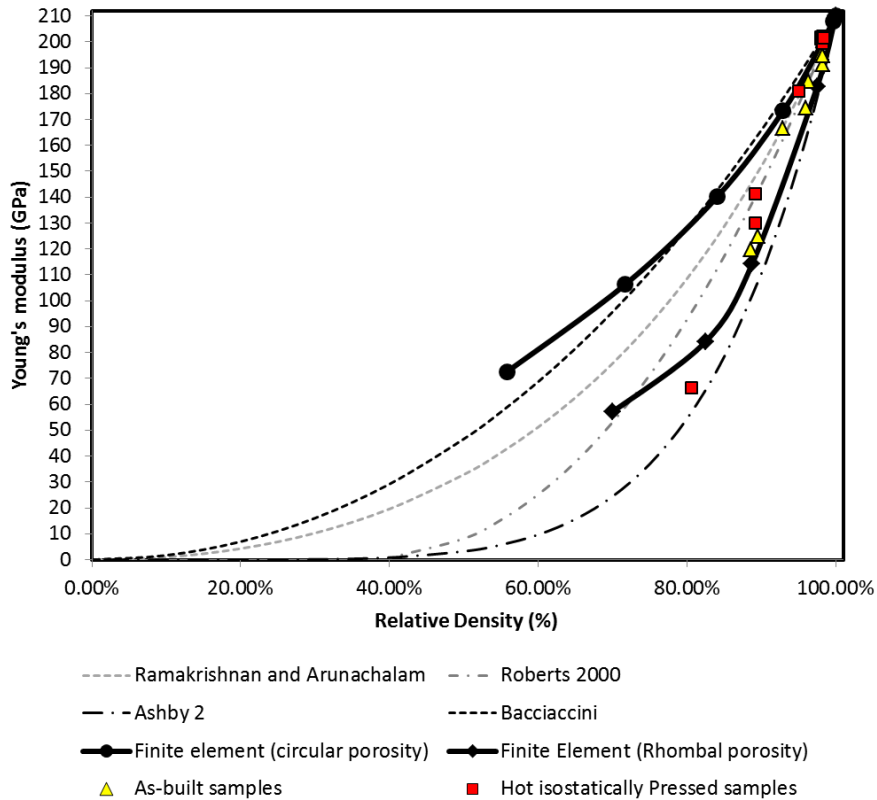
Figure 33 – Young's modulus as a function of relative density, comparing theoretical, measured and finite element results.
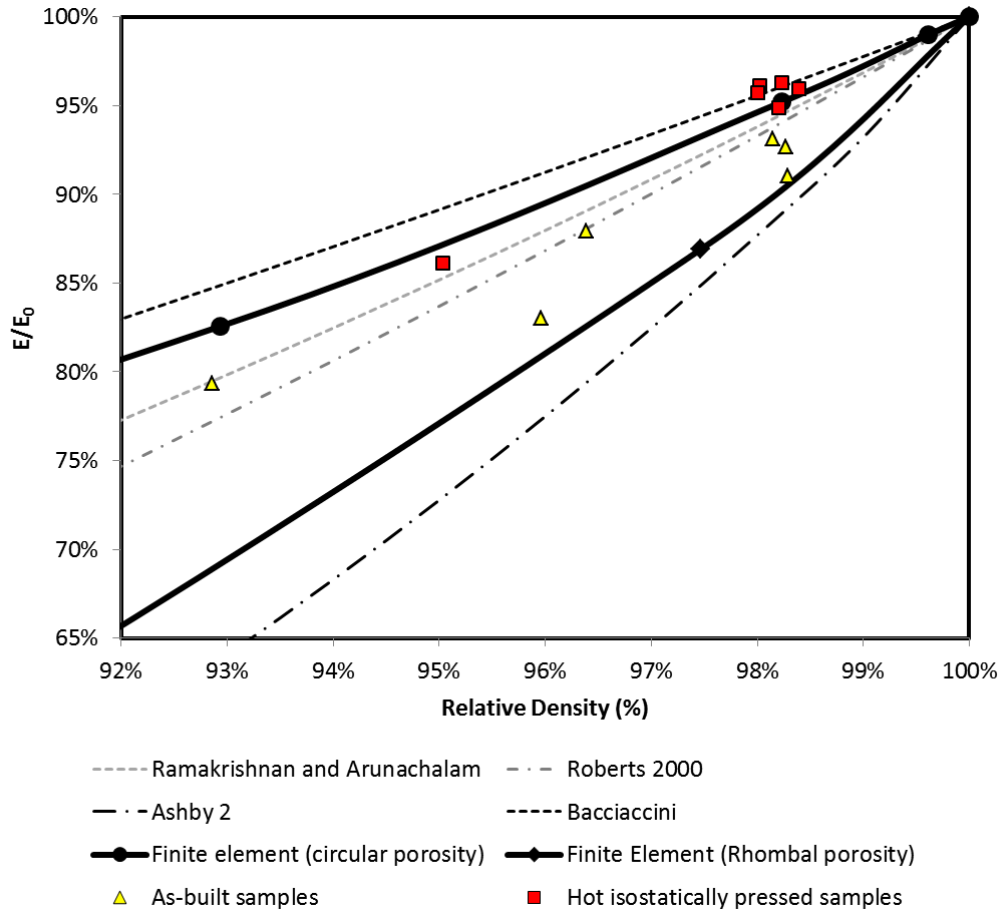
Figure 34 – Normalised Young's modulus (E/E0) as a function of relative density, comparing theoretical, measured and finite element results.

Table 1 – Composition (in wt.%) of 316L powder used in this study.

Grade 316L	Fe	C	Si	Mn	P	S	Cr	Ni	Mo	N	Cu	O
Min	Bal	-	-	-	-	-	17.5	12.5	2.25	-	-	-
Max		0.03	0.75	2	0.025	0.01	18	13	2.5	0.1	0.5	0.1
Actual		0.019	0.67	1.45	0.019	0.006	17.9	12.7	2.36	0.06	0.2	0.022

Table 2 – Parameter settings with corresponding laser energy density (Equation 2 - J/mm^3), laser line speeds (mm/s) and normalised enthalpy (Equation 10, [56]).

Exposure time (μs)	Point Distance (μm)											
	A - 25 μm				B - 65 μm				C - 105 μm			
	Ref	J/mm^3	mm/s	$\frac{\Delta H}{h_s}$	Ref	J/mm^3	mm/s	$\frac{\Delta H}{h_s}$	Ref	J/mm^3	mm/s	$\frac{\Delta H}{h_s}$
70 μs	A1	81.29	357	4.4	B1	32.27	928	2.7	C1	19.35	1500	2.1
110 μs	A2	127.74	227	5.5	B2	49.13	590	3.4	C2	30.41	954	2.7
150 μs	A3	174.19	166	6.4	B3	65.41	433	4.0	C3	40.49	700	3.1

Table 3 – Relative density measurements of the 316L cubes for as-built and post HIP cycle (1200C, 100MPa, 4 hours). The absolute density of 316L steel is taken as 7.99 g/cm^3.

Sample ref.	Laser input energy (J/mm^3)	Pre-HIP Relative density (%) Average from gravimetric measurements	Pre-HIP Relative density (%) Average from image analysis	Pre-HIP density (g/cm^3) Average from measurements	Sample ref.	Post-HIP Relative density (%) Average from gravimetric measurements	Post-HIP Relative density (%) Average from image analysis	Post-HIP density (g/cm^3) Average from measurements
A1-1	81.29	98.35% ±0.52		7.859 ±0.04	A1-1H	98.23% ±0.78	100.00% ±0.00	7.848 ±0.06
A1-2	81.29	98.29% ±0.37	99.63% ±0.40	7.854 ±0.03				
A1-3	81.29	98.27% ±0.51		7.852 ±0.04				
A2-1	127.74	95.96% ±0.77		7.667 ±0.06				
A2-2	127.74	96.21% ±0.33		7.687 ±0.03	A2-2H	98.20% ±1.04	100.00% ±0.00	7.846 ±0.08
A2-3	127.74	96.95% ±0.64	98.02% ±2.40	7.746 ±0.05				
A3-1	174.19	93.61% ±1.28		7.480 ±0.10	A3-1H	98.39% ±0.93	100.00% ±0.00	7.861 ±0.07
A3-2	174.19	93.63% ±1.48	95.82% ±2.66	7.481 ±0.12				
A3-3	174.19	92.86% ±1.41		7.420 ±0.11				
B1-1	31.27	89.60% ±0.73		7.159 ±0.06	B1-1H	89.22% ±0.87	93.39% ±1.12	7.129 ±0.07
B1-2	31.27	89.60% ±0.59		7.159 ±0.05				
B1-3	31.27	89.51% ±0.66	87.06% ±1.88	7.152 ±0.05				
B2-1	49.13	98.15% ±0.92		7.842 ±0.07				
B2-2	49.13	97.81% ±1.23		7.815 ±0.10	B2-2H	98.02% ±0.78	99.99% ±0.00	7.832 ±0.06
B2-3	49.13	98.16% ±0.91	99.18% ±0.50	7.843 ±0.07				
B3-1	67.00	98.35% ±0.89	99.64% ±0.21	7.858 ±0.07				
B3-2	67.00	98.31% ±0.74		7.855 ±0.06	B3-2H	98.00% ±0.69	99.99% ±0.01	7.830 ±0.06
B3-3	67.00	98.29% ±1.01		7.853 ±0.08				
C1-1	19.35	77.97% ±0.09		6.230 ±0.01	C1-1H	80.60% ±2.00	87.92% ±3.03	6.440 ±0.16
C1-2	19.35	78.25% ±1.06	59.53% ±8.44	6.523 ±0.47				
C1-3	19.35	77.09% ±0.28		6.160 ±0.02				
C2-1	30.41	90.14% ±0.72	85.24% ±5.82	7.202 ±0.06				
C2-2	30.41	89.57% ±0.68		7.157 ±0.05	C2-2H	89.18% ±0.99	94.13% ±0.97	7.125 ±0.08
C2-3	30.41	88.65% ±0.75		7.083 ±0.06				
C3-1	41.47	96.39% ±1.15		7.702 ±0.09				
C3-2	41.47	96.22% ±0.98	97.31% ±0.93	7.688 ±0.08				
C3-3	41.47	95.48% ±0.80		7.629 ±0.06	C3-3H	95.03% ±1.78	97.65% ±0.98	7.593 ±0.14

Table 4 – Porosity measurements from microscope image analysis taken from 5 positions per sample.

Sample	P1	P2	P3	P4	P5	Average porosity (%)	Average Perimeter (µm)	Average Circularity (%)	Average Feret Diameter (µm)
A1-2	0.13%	0.51%	0.08%	0.13%	1.01%	0.37 ±0.40	20.24	91.84%	6.51
A2-3	6.17%	1.30%	0.34%	0.48%	1.63%	1.98 ±2.40	49.39	88.90%	14.89
A3-2	3.22%	7.41%	2.35%	1.36%	6.55%	4.18 ±2.66	47.73	83.90%	15.36
B1-3	14.01%	14.51%	14.34%	11.37%	10.46%	12.94 ±1.88	79.45	72.80%	18.75
B2-3	1.29%	1.18%	0.30%	0.27%	1.08%	0.82 ±0.50	17.69	88.70%	5.27
B3-1	0.49%	0.17%	0.09%	0.56%	0.47%	0.36 ±0.21	22.74	88.30%	6.40
C1-2	40.34%	54.07%	30.87%	38.57%	38.51%	40.47 ±8.44	54.88	79.80%	16.43
C2-1	21.83%	6.00%	16.66%	16.26%	13.06%	14.76 ±5.82	118.91	74.90%	26.59
C3-2	2.50%	2.03%	1.64%	3.78%	3.50%	2.69 ±0.93	90.29	78.40%	21.32
A1-1H	0.00%	0.00%	0.00%	0.00%	0.00%	0.00 ±0.00	12.97	74.20%	3.37
A2-2H	0.00%	0.00%	0.00%	0.00%	0.00%	0.00 ±0.00	11.73	74.20%	3.39
A3-1H	0.00%	0.00%	0.00%	0.00%	0.00%	0.00 ±0.00	11.17	76.00%	3.16
B1-1H	5.80%	8.05%	5.39%	6.37%	7.48%	6.61 ±1.12	71.68	72.20%	18.65
B2-2H	0.02%	0.01%	0.02%	0.01%	0.01%	0.01 ±0.00	11.85	77.80%	4.85
B3-2H	0.02%	0.01%	0.01%	0.01%	0.02%	0.01 ±0.01	13.32	87.00%	4.51

C1-1H	10.34%	9.82%	14.38%	16.23%	9.65%	12.08 ±3.03	128.34	71.60%	29.82
C2-2H	4.28%	6.75%	5.67%	6.22%	6.42%	5.87 ±0.97	101.89	70.70%	28.76
C3-3H	3.80%	2.85%	1.52%	2.10%	1.48%	2.35 ±0.98	62.51	75.30%	18.32

Table 5 – Average measured longitudinal and shear wave velocities as measured with the ultrasound gauge for as-built and hot isostatically pressed cubes (LOS = Loss of signal).

Sample	Laser Energy Density (J/mm^3)	Density (kg/m^3)	Relative density	Average VL (m/s)	Average VT (m/s)	Poisson's ratio ν	Young's modulus (GPa)	Shear modulus (GPa)
A3-3	174.19	7480.57	93.62%	5460.50±50.29	2943.00±25.02	0.295 ±0.001	166.63 ±4.0	64.08 ±1.3
A2-1	127.74	7668.02	95.97%	5595.75±41.74	2964.75±125.36	0.305 ±0.022	174.34 ±14.7	66.71 ±6.7
A1-3	81.29	7842.51	98.15%	5645.00±12.41	3099.25±40.38	0.284 ±0.007	194.57 ±4.5	75.88 ±2.2
B3-3	67.00	7824.60	97.93%	5661.50±47.13	3066.75±61.60	0.292 ±0.006	191.19 ±7.0	74.02 ±3.1
B2-1	49.13	7796.09	97.57%	5546.50±85.96	3121.25±20.45	0.268 ±0.007	195.54 ±7.0	76.21 ±1.2
B1-2	31.27	7104.61	88.92%	4440.00±85.97	2667.25±45.88	0.218 ±0.008	124.78 ±6.2	50.48 ±1.9
C2-3	30.41	7052.31	88.26%	4347.50±72.38	2629.75±26.85	0.211 ±0.008	119.68 ±4.6	48.71 ±1.1
C3-1	41.47	7629.79	95.49%	5387.75±25.01	3091.00±68.34	0.255 ±0.013	184.65 ±6.4	73.69 ±3.3
C1-3	19.35	6144.86	76.91%	LOS	LOS	LOS	LOS	LOS
A1-1H	81.29	7885.70	98.69%	5681.25±46.31	3147.75±40.34	0.288 ±0.009	202.23 ±12.4	76.94 ±2.3
C1-1H	19.35	6624.52	82.91%	3387.00±80.29	2043.75±22.41	0.210 ±0.001	66.48 ±3.6	27.44 ±1.5
C2-2H	30.41	7136.79	89.32%	4754.75±290.96	2855.75±128.52	0.218 ±0.020	141.23 ±19.7	56.01 ±5.2
A3-1H	174.19	7912.35	99.03%	5724.75±15.82	3140.50±72.73	0.295 ±0.003	201.53 ±13.9	77.15 ±4.6
A2-2H	127.74	7897.91	98.85%	5694.00±30.84	3098.50±27.72	0.297 ±0.013	199.26 ±14.7	74.83 ±1.4
B3-2H	67.00	7893.70	98.79%	5659.25±32.43	3201.75±80.39	0.272 ±0.012	201.02 ±9.7	78.92 ±4.6
C3-3H	41.47	7709.97	96.50%	5403.75±47.85	3119.75±45.75	0.255 ±0.016	180.84 ±9.0	71.97 ±4.5
B2-2H	49.13	7901.79	98.90%	5644.50±17.02	3182.25±66.64	0.271 ±0.007	201.79 ±10.4	78.53 ±3.7

Table 6 – Tensile properties for 316L from other publications

Reference	Process	Heat treatment	Laser power / speed	Relative density	Young's modulus (GPa)	Yield Strength (MPa)	Upper tensile strength (MPa)	Elongation at failure (%)
This work	AM250	None	180W 600 mm/s	98.04%	195.54±7.0	385	524	22%
This work	AM250	HIP 1125°C 137MPa	180W 600 mm/s	98.90%	201.79±10.4	227	542	41%
Mower et al., [20]	EOS M270	None	195W 750 mm/s	-	180-193	496-473	680-717	28-30%
Zhang et al., [30]	SLM250	None	100W 300 mm/s	98-99.7%	-	-	500-600	10%
Carlton et al., [32]	Concept M2	None	85W 400 mm/s	97.6%	-	-	540±120	44%
Carlton et al., [32]	Concept M2	Annealed	85W 400 mm/s	97.6%	-	375	490	51%
Carlton et al., [32]	Concept M2	None	85W 222 mm/s	99.9%	-	590±17	705±60	44%
Carlton et al., [32]	Concept M2	Annealed	85W 222 mm/s	99.9%	-	375	555	51%
Spierrings et al., [13], [34]	Concept	None	104W 450 mm/s	99%	-	640	760	30%
Tolosa et al., [69]	SLM 250 Realizer	None	200W 1000 mm/s	99.9%	-	-		
Saiedi, [47]	EOS M270	As-built	190W 800 mm/s	98.6%	-	456	703	45%
Saiedi, [47]	EOS	Annealed	190W 800	98.6%	-	419	674	51%

Saiedi, [47]	M270 EOS M270	HIP	190W 800 mm/s	99.7%	-		220	570	54%
Tolosa et al., [69]	Wrought	None	-	-	-		220–270	520–680	40–45%
Yadolahi et al., [33]	LENS	None	360W 8.5 mm/s	-	-		405-415	620-660	32-40%
Ledbetter et al., [62]	Hot rolled	None	-	-	194-195		-	-	-
Shankar et al., [66]	Hot rolled	None	-	-	7.849	196.79±0.4	-	-	-
Song et al., [52]	Hot rolled	Treated	-	-	-		245	585	61.20%
Song et al., [52]	Hot rolled	As-rolled	-	-	-		220	565	64.50%
Kurgen et al.,	P/M cold compact	None	-	-	-		-	300	-
ASM Handbook, [74]	Cast CF-3M	1045°C WQ	-	-	-		262	552	55%
Busby et al., [71] ITER	Cast CF-3M	None	-	-	-		261±28	555.6±24	55.1%±0.4